Base Flow and Heat Transfer Characteristics of a Four-Nozzle Clustered Rocket Engine: Effect of Nozzle Pressure Ratio

R. Nallasamy[1] and M. Kandula[2]
ASRC, Kennedy Space Center, FL 32899

L. Duncil[3] and P. Schallhorn[4]
NASA Kennedy Space Center, FL 32899

The base pressure and heating characteristics of a four-nozzle clustered rocket configuration is studied numerically with the aid of OVERFLOW Navier-Stokes code. A pressure ratio (chamber pressure to freestream static pressure) range of 990 to 5,920 and a freestream Mach number range of 2.5 to 3.5 are studied. The qualitative trends of decreasing base pressure with increasing pressure ratio and increasing base heat flux with increasing pressure ratio are correctly predicted. However, the predictions for base pressure and base heat flux show deviations from the wind tunnel data. The differences in absolute values between the computation and the data are attributed to factors such as perfect gas (thermally and calorically perfect) assumption, turbulence model inaccuracies in the simulation, and lack of grid adaptation.

Nomenclature

a	velocity of sound, ft/s
c_p	specific heat at constant pressure, Btu/(lb_m °R)
D_b	base diameter, in.
D_e	nozzle exit diameter, in.
D_s	nozzle spacing, in.
D_s / D_e	nozzle spacing ratio
d	disk thickness, ft
e	internal energy per unit mass, Btu/lb_m
J	Jacobian of coordinate transformation
L	nozzle extension, distance of exit plane from base plate, in.
L / D_e	nozzle extension ratio
M	Mach number
P_c	combustion chamber pressure, lb_f/ft^2 abs
P_c / p_o	engine nozzle pressure ratio
p	static pressure, lb_f/ft^2 abs.
p_o	freestream static pressure, lb_f/ft^2 abs
Q	conservative variable vector

---

[1]Mail Stop: ASRC-5211, Senior Member AIAA.
[2]Subject Matter Expert, Mail Stop: ASRC-5211, Associate Fellow AIAA
[3] Thermal & Environments Engineer, Launch Services Program, Member AIAA
[4] Chief, Thermal & Environments Branch, Launch Services Program, Senior Member AIAA

This material is declared a work of the U.S. Government and is not subject to copyright protection in the United States

q	heat flux, Btu/(ft^2.sec)
r	radial coordinate
R	radius of model base, in.
R_e	Reynolds number
T	temperature, °R
T_c	combustion chamber temperature, °R
T_g	gas temperature near the base, °R
T_d	disk temperature, °R
t	time, s
u, v, w	velocity components
u^*	friction velocity, $\sqrt{\tau_w / \rho}$
x, y, z	physical coordinates
x^+	$x u^* / \nu$
ξ, η, ζ	computational coordinates
γ	ratio of specific heats
ρ	density
γ_n	ratio of specific heats within the nozzle flow

Nondimensional quantities

$p' = p/(\gamma_\infty p_\infty)$
$T' = T/(\gamma_\infty T_\infty)'$
$u' = u / a_\infty$
$v' = v / a_\infty$
$w' = w / a_\infty$
$e' = e / a_\infty^2$

Subscript

∞ - freestream

I. Introduction

A detailed understanding of the afterbody base pressure and heat transfer of launch vehicles with clustered rocket engines is important for afterbody structural design, flight performance and vehicle controllability. In high speed aerodynamic flight of rockets, missiles and projectiles, the base drag forms a substantial component of the total drag. For example, for a typical projectile at Mach 0.8 without drag control, base drag represents 50 percent of the total drag (Sahu and Nietubicz[1]). Also, excessive base heating has become a concern for many launch vehicles.[2]

Multi-nozzle rocket clusters, widely considered for booster configurations, offer many advantages[3,4]. First, they have less total nozzle length compared to single nozzle. Second, they offer controllability in pitch, yaw, and roll by swiveling the individual nozzle. Third, additional thrust at high altitudes and in space is gained by *increasing the base pressure* of the rocket vehicle. At low altitudes, the flow in the base region is accelerated in the downstream direction by the ejector action of the rocket exhaust (Fig. 1). However, at high altitudes, the exhaust of individual nozzles spreads further, resulting in mutual jet impingement with oblique shock generation in between the exhausts. Since parts of the mixing zones surrounding the individual nozzle exhaust do not have sufficient energy to proceed

downstream through the shock wave system into the high pressure area some of the gas in the mixing zone is turned back to flow toward the base of the vehicle[4] and from there outward to the freestream. This can result in *overheating* of the vehicle base and individual engines.

In the past, several experimental and computational fluid dynamics (CFD) studies have been carried out to understand base flow characteristics of clustered nozzle rocket systems. Notable experimental studies on base flow include those of Gothert[3], Gothert and Matz[4], and Brewer and Craven[6]. The base flow and heat transfer characteristics for a four-nozzle cluster at freestream Mach numbers from 2 to 3.5 were reported by Musial and Ward[6].

With regard to numerical analysis of base flowfield, Dougherty and Johnson[8] performed CFD computations and compared their results with the cold flow data of Gothert and Matz[4]. Wang[2] reported Navier-Stokes analysis and compared the predictions with the cold flow data of Brewer and Craven[6]. Ideal gas assumption was used. Grid resolution and turbulence model were found to be important for the accuracy of the predictions. Grid adaptation improved the accuracy of the results[9]. Chern et al.[10] studied multibody base flow afterbody skirts (with single and multiple nozzles) and obtained satisfactory comparisons with the wind tunnel base pressure data of Charezenko et al[11]. Recently Kawai and Fujii[12] reported results of a computational study of cylindrical base flows over a range of subsonic and supersonic speeds.

It is observed that most of the computational analyses reported have focused mainly on the base pressure with relatively less emphasis on base heating. In a recent study (Nallasamy et. al[13]. the present investigation, a CFD analysis of a four-nozzle clustered rocket system configuration is carried out to predict both base pressure and base heating at a pressure ratio of 990, a freestream Mach number of 2.5, and a freeatream Reynolds number of 0.5245×10^6. The present study extends the above analysis for a wide range of pressure ratios from 990 to 5920. The predicted base flow characteristics are compared with the available wind tunnel data of Musial and Ward[7].

II. Experimental Data of Musial and Ward for CFD Validation

Musial and Ward[7] conducted experiments on a wind tunnel model (Fig. 2a) for several four-nozzle clustered configurations (Fig. 2b and 2c). The basic model used in this investigation was a strut mounted cone-cylinder body having a maximum diameter of 12 inches. They conducted tests on two sets of nozzles, bell shaped and conical nozzles. The bell nozzle (Fig. 2d) had an area ratio of 12 and an exit diameter of 2.94 inch while the conical nozzle had area ratio of 6.9 and an exit diameter of 2.2 inches. They studied three different nozzle extension ratios (nozzle extension length from the base to diameter, L/D_e) and different nozzle spacing ratios (nozzle spacing to nozzle exit diameter, D_s/D_e), see Fig. 2c. Each motor was designed to produce a nominal thrust of 500 lbs at a chamber pressure of 600 psia and an estimated chamber temperature of 5350° F. All motors had water cooled jackets. A coaxial tube injector is used in which the fuel (JP-4) is injected through the annulus surrounding each oxidant (liquid oxygen) tube. The data cover freestream Mach numbers from 2 to 3.5 over a range of altitudes 47000 to 100000 ft, corresponding to chamber pressure to freestream static pressure ratios from 340 to 6800.

The rocket engine was maintained at steady operating conditions for 10 seconds. All base plates were uncooled and coated with aluminum oxide insulation. Gas temperatures in the base region were measured by platinum-rhodium thermocouples which extended to 0.5 inch from the base plate. Base static pressures were measured by pressure transducers. Disk calorimeters were used to measure the local heat flux in the base region. Disk temperatures were measured 100 times a second, while other engine parameters were recorded every 2.7 seconds. Heat flux was calculated every 0.75 sec. from the slope of the disk temperature-time curve by the following equation.

$$q = (\rho c_p d)_{disk} \left(dT_d / dt \right) \tag{1}$$

where ρ, c_p and d are the disk density, specific heat and thickness respectively, which are constant for any particular disk at a given temperature. The heat fluxes reported correspond to the maximum measured values at an average disk temperature of 150° F for a given base location. However, during the test, the disk temperature rises from 80° F to about 650° F as shown in Fig. 3, reproduced here from Fig. 6 of reference 6.

III. Geometric Configuration

Figs. 2b and 2c show the four-nozzle clustered rocket system configuration with a nozzle spacing ratio, D_s/D_e of 2.18 and a nozzle extension ratio, L/D_e of 0.7015, chosen for the present investigation corresponding to one of the experimental configurations of reference 6 (See section 2 above). The bell nozzle with an area ratio of 12 was chosen which had a nozzle exit diameter of 2.94 inches. Although, from symmetry considerations it is adequate to solve $1/8^{th}$ sector of the base, it became necessary to solve one quadrant of the base (Fig. 2d) due to a difficulty with volume grid generation

IV. Grid Generation

Overset grid methodology[14] in conjunction with OVERFLOW[15-17] Navier-Stokes code is considered here. A large-scale Chimera grid system application is presented in Slotnick et al[18] demonstrating the usefulness of this methodology to complex configurations. Surface and volume grids (Figs. 4-5) are generated using Gridgen code[19]. An inflow development region for the boundary layer is provided by an extension of the base grid (Fig. 4a). The nozzle surface grid and its downstream extension are shown in Fig. 4b. In the intersection region of the nozzle with the base, a collar grid is generated (Fig. 4c). The collar surface grid is built with the well known chimera grid tools[20] which includes HYPGEN hyperbolic grid generation package. Starting from the intersection curve of nozzle/base surfaces, surface grids are generated on the base and the nozzle. Fig. 4d displays a view of the surface grids for the base, nozzle, and collar. A view of the composite grid of the base, nozzle, and collar is illustrated in Fig. 4e. Collar grids provide the communication between the intersecting grids, as well as necessary resolution for viscous flow computation. A more detailed discussion on collar grids may be found in Parks et al.[21] Field or volume grids are generated using Gridgen and Hypgen packages. Intergrid boundary communication is established with the aid of PEGSUS software[22].

Care was taken to have sufficient grid density near the solid base, in the nozzle shear layer, and near field region. To be able to accurately compute base heat flux and to predict the plume impingement reverse flow region, sufficient resolution near the base surface region was incorporated. Table 1 shows the sizes of component field grids. There are a total of over 2.4 million grid points to represent one quadrant of the flowfield of the four-nozzle clustered rocket configuration. A view of the composite volume grids of the base, nozzle, and collar is illustrated in Fig. 5 (in this figure base extension has been excluded for clarity). Based on the Phase I study an upstream extension of 4R was used for all the cases considered here.

The first grid cell normal to the base wall is at $\Delta x/L_{ref} = 10^{-5}$ with $x^+ \sim 0.05$ (where $x^+ = x u^* / \nu$), providing adequate resolution for the accurate calculation of wall heat flux. Unfortunately, neither grid convergence (doubling the number of grid points) nor grid adaptation was considered due to constraints on resources.

V. Numerical Solution

A. Solution algorithm

The three-dimensional compressible Navier-Stokes Code OVERFLOW[15-17] developed by NASA is employed in the present investigation. It solves the governing mean flow equations in conservation form in generalized coordinates (ξ, η, ζ) that are transformations of the rectangular coordinate space (x, y, z). The present solutions are based on the diagonalized version of the Beam-Warming three-factor approximate factorization scheme[23]. Central difference is considered for the inviscid and viscous fluxes. The compressible Navier–Stokes equations solved in OVERFLOW are written in conservation law form as:

$$\frac{\partial}{\partial t}\left(\frac{Q}{J}\right)+\frac{\partial \hat{F}}{\partial \xi}+\frac{\partial \hat{G}}{\partial \eta}+\frac{\partial \hat{H}}{\partial \varsigma}=\frac{1}{\mathrm{Re}}\left[\frac{\partial \hat{F}_{\upsilon}}{\partial \xi}+\frac{\partial \hat{G}_{\upsilon}}{\partial \eta}+\frac{\partial \hat{H}_{\upsilon}}{\partial \zeta}\right] \tag{2}$$

where $Q=(\rho',\rho'u',\rho'v',\rho'w',e')$ is the vector of conservative variables, J is the geometric transformation Jacobian, $\hat{F}$, $\hat{G}$, and $\hat{H}$ are inviscid fluxes, and $\hat{F}_\upsilon$, $\hat{G}_\upsilon$, and $\hat{H}_\upsilon$ are the viscous fluxes. Here the primes denote nondimensional quantities as specified in the OVERFLOW code.

B. Turbulence model

The validity of CFD analysis is critically dependent on the choice of turbulence model. Both one- and two-equation turbulence models are implemented in the OVERFLOW code. Two-equation models provide better flow physics[24] than one-equation models with regard to adverse pressure gradients, flow separation, etc. However, for practical applications involving three-dimensional (3-D) flows, one-equation models are frequently considered.

The one equation models of Spalart-Allmaras[25] and Baldwin-Barth[26] are available in the OVERFLOW code. In these models, an equation for turbulent kinetic equation is solved. Kandula and Buning[27] examined the afterbody-exhaust jet flowfield with the aid of Baldwin-Barth turbulence model, and obtained satisfactory distribution of the surface pressure except in the separated flow region. Baldwin-Barth model is considered for the present study. (Since a solution obtained with Spalart-Allmaras turbulence model showed a non-physical flow pattern, it is not used here).

C. Initial and boundary conditions

Initially, the flow velocities in all the grids were set to zero. On the base surface, no slip condition for the velocity and constant wall temperature boundary condition were specified. At the inflow boundary upstream of the base uniform inflow conditions were prescribed. Nozzle exit flow conditions were derived from one-dimensional isentropic flow corresponding to the stagnation pressure and temperature. A velocity profile that incorporated shear layer at the nozzle lip line was specified. The flow properties at the exit boundary of the nozzle grid were extrapolated from those of the interior domain. An axis boundary condition was considered for the nozzle centerline.

D. Flow conditions

In the present investigation, six pressure ratios, Pc/Po (chamber pressure to freestream static pressure) are considered. Table 2 provides the nozzle geometry considered in this study and Table 3 lists the freestream conditions for all the pressure ratios. Base wall temperature was specified as 150° F for all the six cases. This value represents the average disk temperature at which the maximum heat flux was measured in the wind tunnel experiments as indicated earlier.

E. Gas models

Whereas the freestream is treated as a perfect gas with γ=1.4, a value of γ=1.3 was considered for the isentropic low within the nozzle. Equivalent nozzle exit conditions are accordingly obtained from the chamber pressure and temperature assuming perfect gas with γ= 1.3. This became necessary since the combustion gases deviate from γ=1.4. In the entire flowfield, perfect gas with γ=1.4 is considered.

VI. Results and Discussion

The numerical solutions reported here were obtained for a range of pressure ratios (P_c/p_o) of 990 to 5920, and a freestream Mach number range of 2.5 to 3.5. Baldwin-Barth one-equation turbulence model is considered.

A. Convergence history

A typical convergence history for the solution residuals is shown in Fig. 6. It required about 12,000 iterations to achieve convergence to steady state.

B. Flowfield

The Mach number contours at the nozzle corner expansion are shown for a pressure ratio of Pc/Po = 990 in Fig. 7. The variation of jet boundary as a function of pressure ratio, relative to that for Pc/Po = 990, is shown in Fig.8. The figure shows an increasing jet expansion with pressure ratio, as is expected.

C. Comparisons with the wind tunnel data

It is recognized that the wind tunnel experimental conditions are somewhat different from those of the present numerical simulation. This test case is chosen here as it appears to be the only one known to the authors where both the base pressure and base heat flux are measured. The following circumstances represent the experimental conditions. All rocket motors had water cooled jackets and all base plates were uncooled and coated with aluminum oxide insulation. Nozzle cooling and radiation losses reduce the base gas temperatures and result in lower values of temperature ratio (gas temperature to chamber temperature) than might be expected. The heat flux reported represent peak values at a given radial location, measured at an average value of disk temperature of 150° F. The temperature-time history plot in Fig. 3 suggests that the disk temperature increased almost linearly from 80° F to 650° F in 10 sec during which steady operating conditions (chamber pressure etc.) of the rockets were maintained. Peak heat flux is measured at some instance within the 10 sec. time frame. The actual base temperature at which the maximum heat flux is measured is uncertain.

In the numerical simulation a steady solution is obtained with the base wall temperature fixed at 150° F. This value represents the average temperature at which maximum heat fluxes were measured in the experiments (which was at one instant during the 10 sec operation of the rocket motors as mentioned above) at each location on the symmetry plane. Nozzle cooling and radiation losses have not been accounted for in the numerical simulation. Thus, the heat transfer rate computed from the CFD solution would be expected to be higher than that of the experiments since the computed gas temperatures would be higher.

Fig. 9 shows measured data for the radial variation of base pressure for the six pressure ratios considered. The low pressure ratios (990, 1280, and 1760) show a tendency for the pressure minimum near r/R=0.6. A relatively sharp rise in the base pressure is noted near the edge of the base for Pc/Po = 990. The three high pressure ratios (2650, 3760, and 5920) produce maximum pressures near the center of the base with the pressure decreasing as the radius increases.

The measured radial variation of heat flux shown in Fig. 10 indicates that the maximum heat flux occurs near the center of the base and decreases with increase in radius. For the range of pressure ratios considered, the maximum heat flux occurs for the highest pressure ratio of 5920. Generally, at any given base radial location, the heat flux increases with an increasing pressure ratio.

Fig. 11 shows the radial variation of base pressure obtained from the OVERFLOW Navier-Sotkes solutions for the six pressure ratios. The base pressure decreases with increasing pressure ratio Pc/Po for the range of pressure ratios considered. For Pc/Po 990 and 1280 the numerical solution predicts a low pressure region (bubble) that is not observed in the data. The reason for this behavior is not clear at this time.

Base heat flux variations from the numerical solutions are plotted in Fig. 12. Here, two distinct sets of curves emerge - one for the three low Pc/Po pressure ratios and the other for the three high pressure ratios. This indicates that the flow pattern on the base is distinctly different for these two ranges of pressures.

Figs. 13-24 show direct comparisons of computed base pressure and heat flux with the measured data for each Pc/Po pressure ratio. Referring to Figs. 13 and 14, at Pc/Po = 990, it is seen that that the pressure bubble region (under-prediction of data) in Fig. 13 corresponds to the high heat flux region near the edge of the base. As the pressure ratio increases, the difference between the predicted base pressure and the measured data increases by as much as to a factor of two. While comparison of predicted base heat flux with the measured values appears slightly better than the base pressure comparison, the peak heat flux predicted near the center of the base is lower than the measured value for all the Pc/Po pressure ratios considered. At high pressure ratios, the predicted heat flux at radii greater than 0.5, are higher than the measured values.

The predicted base pressure and heat flux at radial locations 0.1 and 0.9 are compared with the measured values in Figs. 25 and 26 as a function of Pc/Po pressure ratio. While the predicted trends agree with those of the data (except for the data for Pc/Po=3760 at r/R = 0.1), the absolute values differ. The predicted temperature parameter T_g/T_c (ratio of base gas temperature to chamber temperature, measured at a distance 0.5 inch from the base on a line parallel to it) comparison with the data as a function of pressure ratio is shown in Fig. 27. The figure indicates that for r=0.1, the temperature parameter variation with pressure ratio is in reasonable agreement with the data.

The predicted radial variations of temperature parameter T_g/T_c (ratio of base gas temperature to chamber temperature) at a distance 0.5 inch from the base on a line parallel to it are shown in Fig. 28 for all the six pressure ratios considered. The radial variation of the predicted base temperature parameter also shows two sets of curves - one for low pressure ratios and the other for high pressure ratios similar to that of heat flux curves (Fig. 12). The experimental data are shown in Fig. 29. They show higher values of temperature parameter near the center of the base. Comparisons of the predicted and measured values of the temperature parameter for each pressure ratio are shown in Figs. 30 to 35. Only for high pressure ratios (2650, 3760, and 5920) the predicted temperature parameters show reasonable agreement with the data.

VII. Conclusions

The base pressure and heat transfer characteristics of a four-nozzle clustered rocket engine have been numerically investigated over a wide range of pressure ratio (Pc/Po) with the aid of OVERFLOW compressible Navier-Stokes code. The predicted radial variations of base pressure and base heat flux show qualitative agreement with the wind tunnel data. Significant discrepancies exist between the absolute computed and the measured values. The departures in the absolute values are believed to originate partly from factors such as the ideal gas assumption, accuracy of the turbulence model, uncertainties in the base wall temperature, and lack of grid adaptation.

Acknowledgment

This work was supported by the Launch Services Program (LSP) at Kennedy Space Center with Mr. Leonard Duncil as the task order manager.

References

1. Sahu J., and Nietubicz, C.J., "Navier-Stokes computation of projectile base flow with and without mass injection," AIAA Journal, Vol. 23, 1985, pp. 1348-1355.

2. Wang, T.S., Numerical analysis of base flowfield for a four-engine clustered nozzle configuration, J. Propulsion and power, Vol. 11, pp. 1076-1078, 1995.

3. Gothert, B.H., Base flow characteristics of missiles with clustered rocket exhausts, Aerospace Engineering, pp. 28-117, 1961.

4. Goethert, B.H, and Matz, R., Fluid dynamic aspects of space flight, Vol. II, Experimental investigation of base flow characteristics of four nozzle-cluster rocket model, Gordon and Breach, AGARDograph, 87,1966.

5. Vick, A.R., Cubbage, J.M., and Andrews, E.H., Rocket exhaust-plume problems and some recent related research, in Fluid dynamic aspects of space flight, Vol. II, AGARD, pp. 129-180, 1966

6. Brewer, E.B., and Craven, C.E., Experimental investigation of base flowfield at high altitudes for a four-engine clustered nozzle configuration, NASA TND-5164, 1969.

7. Musial, N.T., and Ward, J.J., Base flow characteristics for several four clustered rocket configurations at Mach numbers 2.0 to 3.5, NASA TM, 1961.

8. Dougherty, N.S., and Johnson, S.L., Four nozzle benchmark wind tunnel USA code solutions for multiple rocket base flow recirculation at 145,000 ft altitude, Report No. N95-23654, Rockwell International Space Systems Division, Huntsville, Alabama.

9. Wang, T.S., Grid resolved analysis of base flowfield for four-engine clustered nozzle configuration, J. of Spacecrafts and rockets, Vol. 33, 1966.

10. Chern, S.Y., Marlatt, S.W., and Colbenson, W.A., Computational simulation on multibody base flow with afterbody skirts and deflected rocket nozzles, AIAA-98-2559, 1998.

11. Charezenko, N., and Hayes, C., Jet effects at supersonic speeds on base and afterbody pressures of a missile model having single and multiple jets, NASA TN D-2046, 1963.

12. Kawai, S, and Fujii, K, Time-series and time-averaged characteristics of subsonic to supersonic base flows, AIAA Journal Vol. 45, pp. 289-301, 2007.

13. Nallasamy, R., Kandula, M., Duncil, L., and Schallhorn, P., (2008) Numerical simulation of the base flow and heat transfer characteristics of a four-nozzle clustered rocket engine, 40th AIAA Themophysics Conference, AIAA-2008-4128.

14. Benek, J.A., Steger, J.L., and Dougherty, F.C., A flexible grid embedding technique with application to the Euler equations, AIAA-83-1944, 1983.

15. Buning, P.G. et al., OVERFLOW User's Manual, Version 1.8s, NASA Langley Research Center, November 1998.

16. Kandula, M., and Buning, P.G., (1994) Implementation of LU-SGS algorithm and Roe upwinding scheme in OVERFLOW thin layer Navier-Stokes code, 25th AIAA Fluid Dynamics Conference, AIAA-94-2357.

17. Jespersen, D., Pulliam, T, and Buning, P., Recent enhancements to OVERFLOW (Navier-Stokes code), AIAA-97-0644. 1997.

18. Slotnik, J.P., Kandula, M., and Buning, P.G., (1994) Navier-Stokes simulations of the space shuttle launch vehicle flight transonic flowfield using large scale Chimera grid system, AIAA-94-1860.

19. Steinbrenner, J., and Chawner, J.R., The Gridgen Version-9 Multiple block grid generation software, MDA Engineering Report 94-01, June 1994.

20. Chan, W.M., Rogers, S.E., Nash, S.M., and Buning, B.G., Users manual for Chimera grid tools (Version 1.0), NASA Ames Research Center, July 1999.

21. Parks, S.J., Buning, P.G., Steger, J.L., and Chan, W.M., Collar grids for intersecting geometric components within the Chimera overlapped grid scheme, AIAA-91-3423, 1991.

22. Suhs, N.E. and Tramel, R.W., PEGSUS 4.0 User's Manual, Calspan Corp./AEDC Operation, June 1991.

23. Beam, R., and Warming, R.F., (1976), An implicit finite difference algorithm for hyperbolic systems in conservation law form, J Computational physics, Vol. 22, pp. 87-110.

24. Kandula, M., and Wilcox, D.C., An examination of k-ω turbulence model for boundary layers, free shear layers, and separated flows, AIAA-95-2317, 1995.

25. Spalart, P.R. and Allmaras, S.R., A one equation turbulence model for aerodynamic flows, AIAA-92-0439, 1992.

26. Balwin, B.S., and Barth, T.J., One-equation turbulence transport model for high Reynolds number wall-bounded flows, NASA TM 102847, 1990.

27. Kandula, M., and Buning, P.G., Evaluation of Baldwin-Barth turbulence model with an axisymmetric afterbody-exhauast jet flowfield, AIAA Journal, Vol. 31, pp. 1723-1725, 1993.

Table 1 Size of component field grids

Grid name	Grid size	Grid points (x10E-6)
Base	169x77x63	0.820
Nozzle	139x90x121	1.514
Collar	121x39x20	0.094
Total		2.428

Table 2 Geometry and flow parameters

Name	value
Geometry Parameter	
Base diameter, D_b	12 inches
Nozzle exit diameter, D_e	2.94 inches
Nozzle spacing ratio, D_s/D_e	2.18
Nozzle extension ratio, L/D_e	0.7015
Nozzle area ratio	12
Flow Conditions	
Base wall temperature (disk temperature), T_d	610 ^{o} R
Chamber pressure, P_c	600 psia
Chamber temperature, T_c	5810° R

Table 3 Chamber pressure to ambient static pressure ratios (P_c/p_o) and freestream conditions.

No.	Pc/Po	Po (psf)	Freestream Mach number	Freestream Reynolds number
1	990	87.3	2.5	0.5245×10^6
2	1280	67.5	3.0	0.4273×10^6
3	1760	49.1	3.0	0.3263×10^6
4	2650	32.6	3.5	0.2607×10^6
5	3760	23.0	3.5	0.1894×10^6
6	5920	14.6	3.5	0.1204×10^6

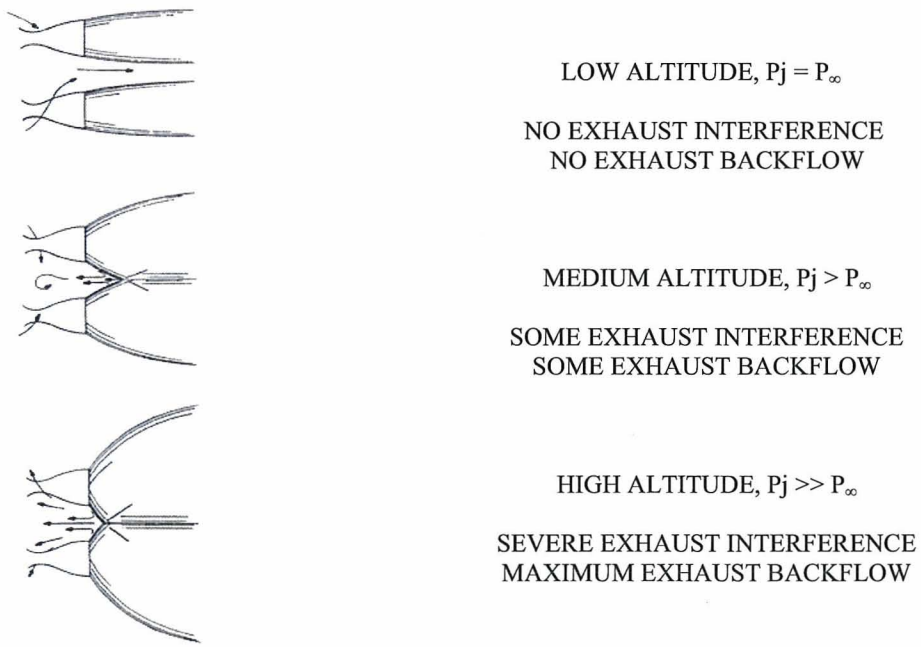

Fig. 1 Multi-nozzle rocket base flow characteristics at different altitudes (Ref. 4).

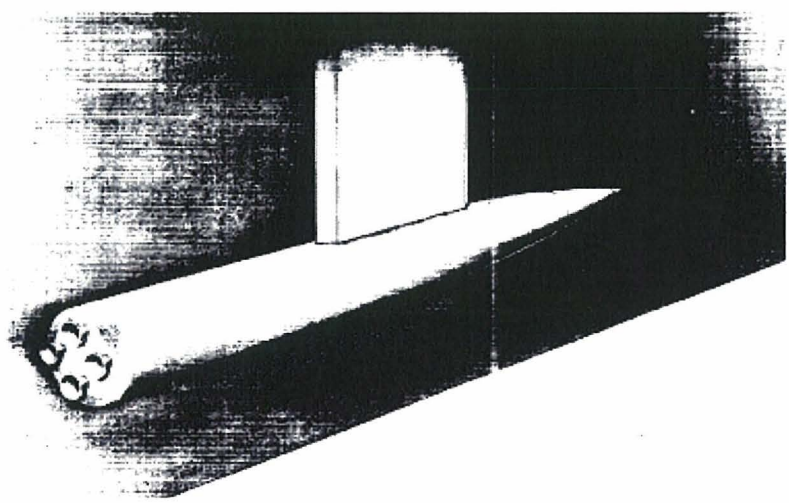

Fig. 2a Base model installed in wind tunnel (Ref. 6)

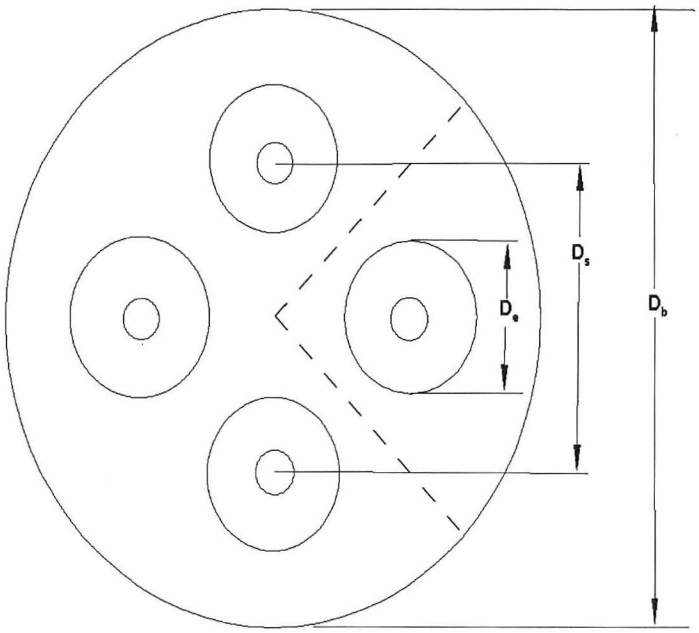

Fig. 2b Four-nozzle configuration: ---- -- symmetry lines where base pressure and heat flux were measured.

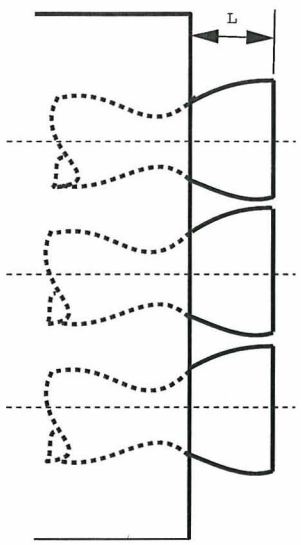

Fig. 2c Variable nozzle extension.

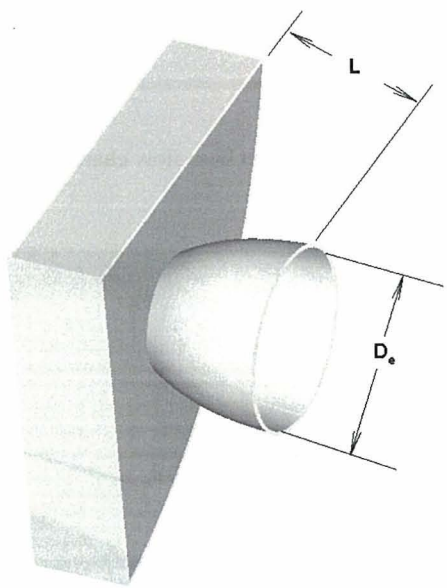

Fig. 2d One quadrant model for the present grid system.

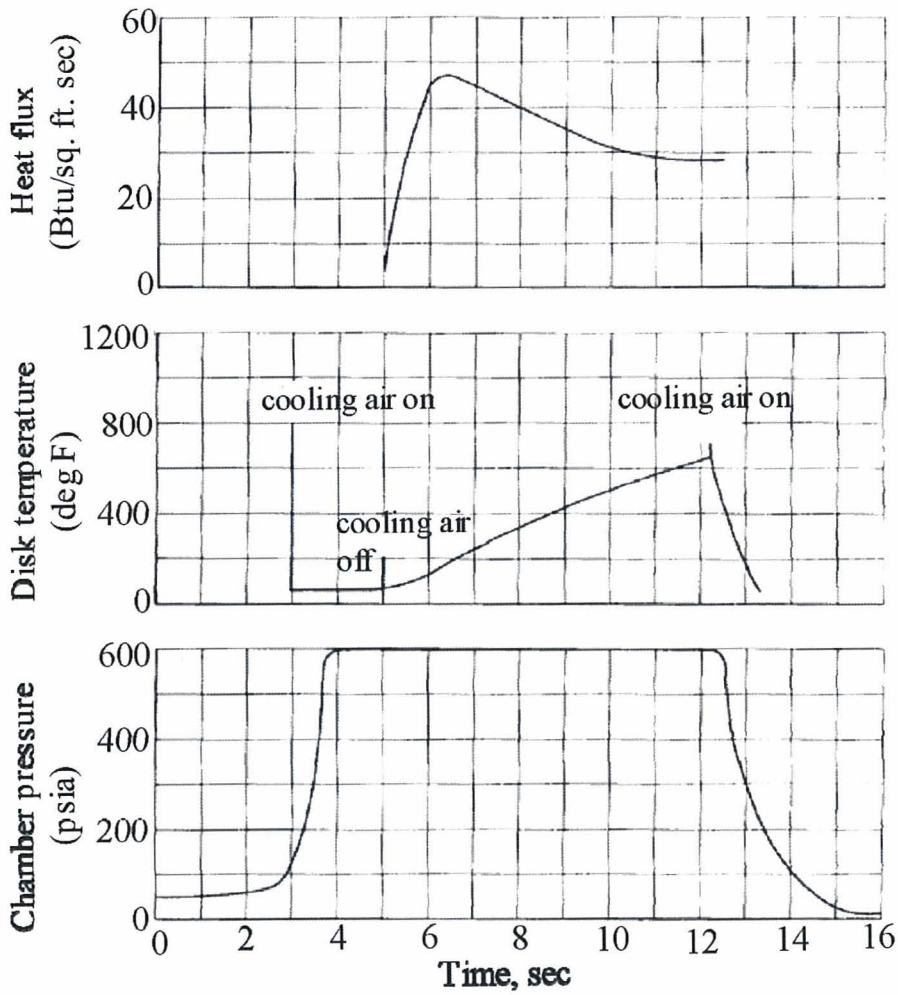

Fig. 3 Typical time histories of engine chamber pressure, disk temperature, and heat flux (Ref. 6)

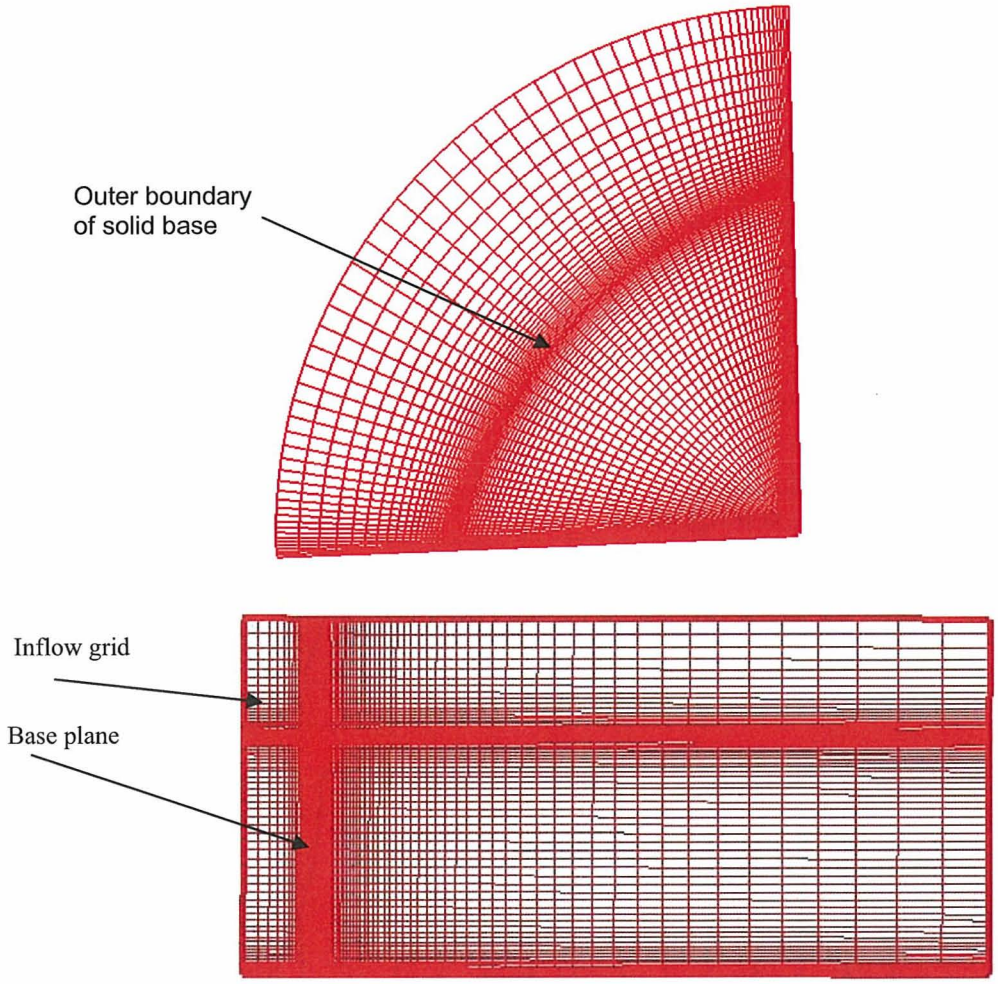

Fig. 4a Base surface grid: two views (partial upstream extension shown).

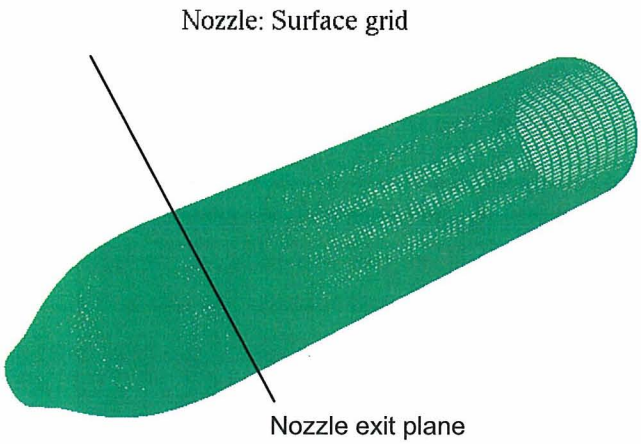

Fig. 4b Nozzle surface grid.

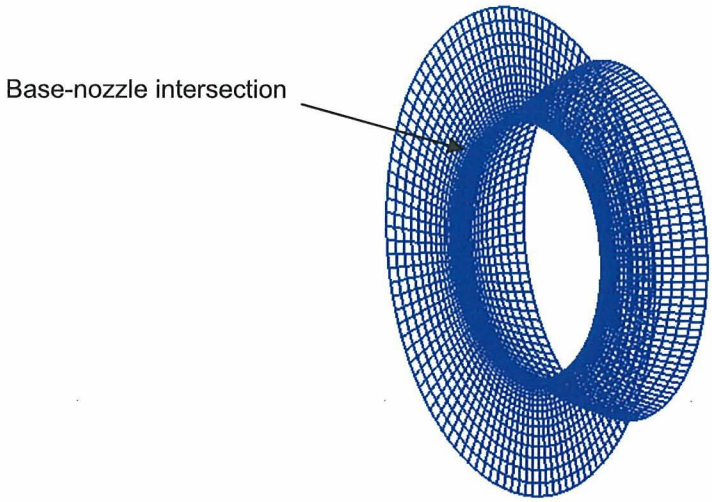

Fig. 4c Collar surface grid.

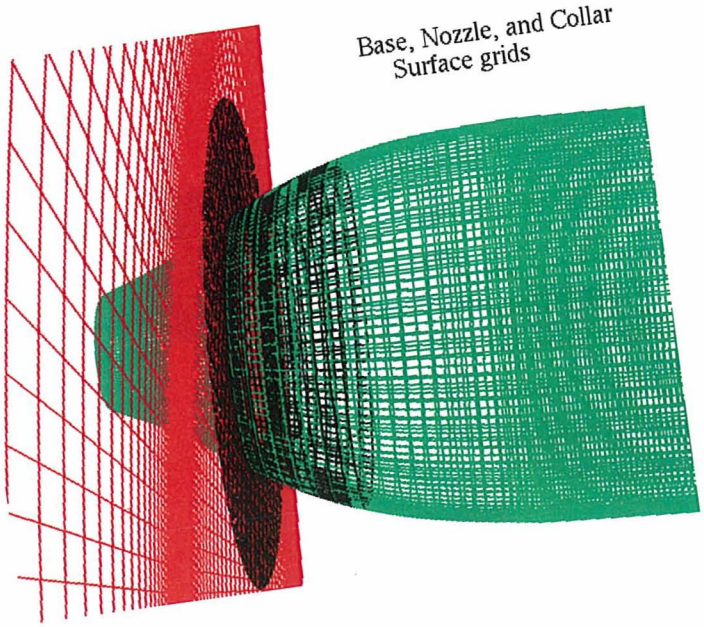

Fig. 4d Surface grids for base, nozzle, and collar.

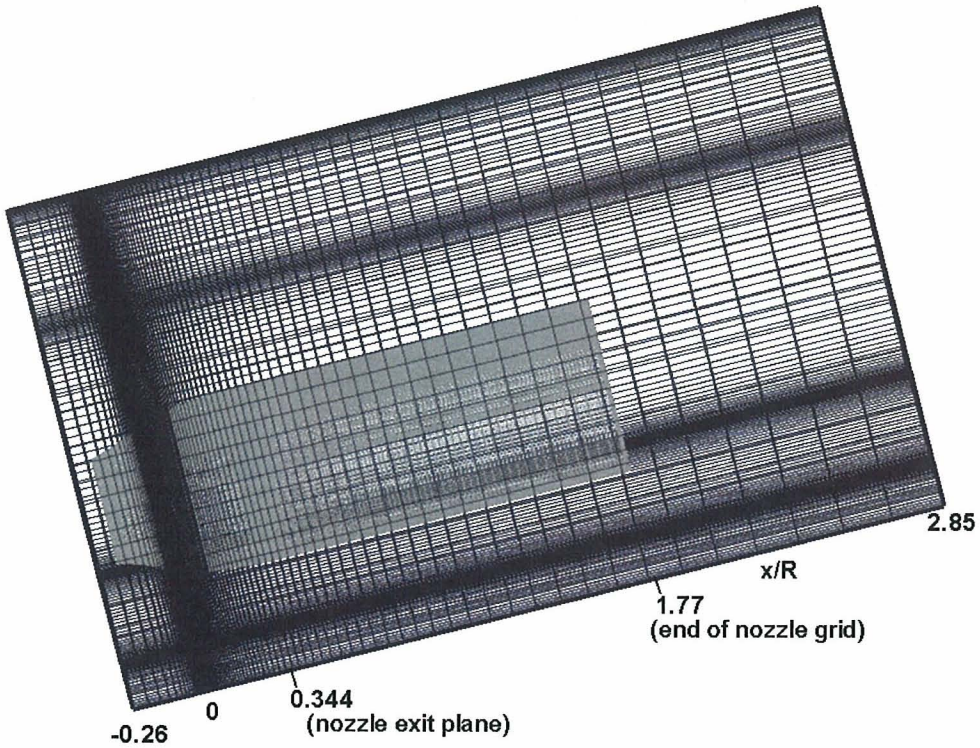

Fig. 4e. A view of composite grid (partial upstream extension shown).

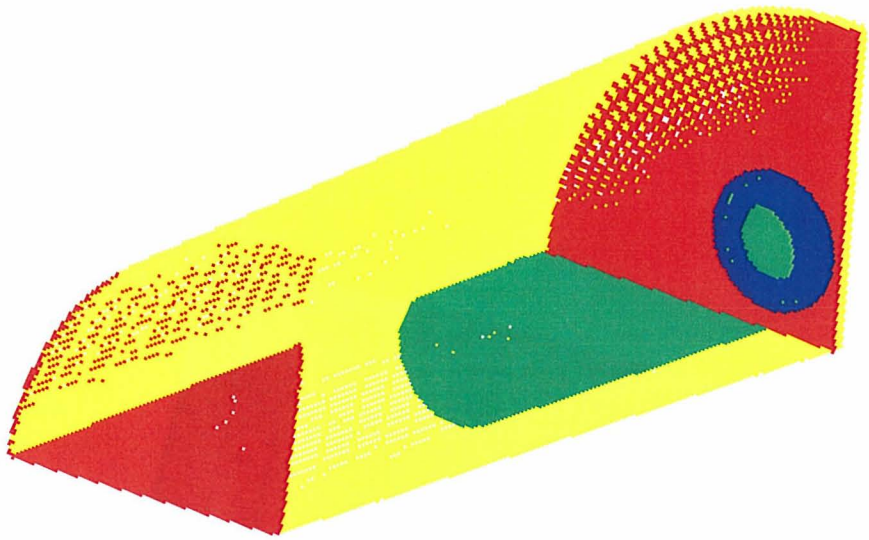

Fig.5 Base, nozzle, and collar volume grids (base extension is excluded for clarity).

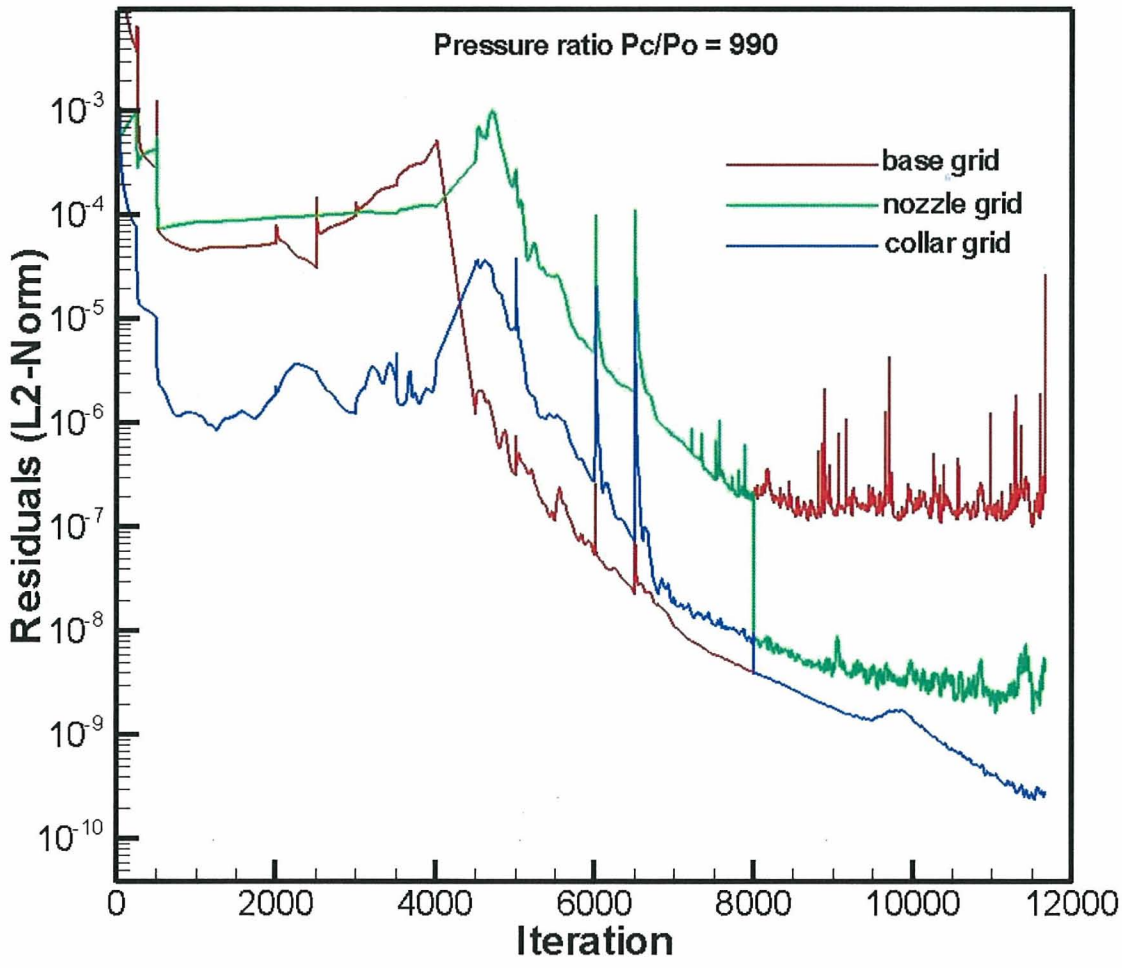

Fig. 6 Residual convergence history for γ =1.3.

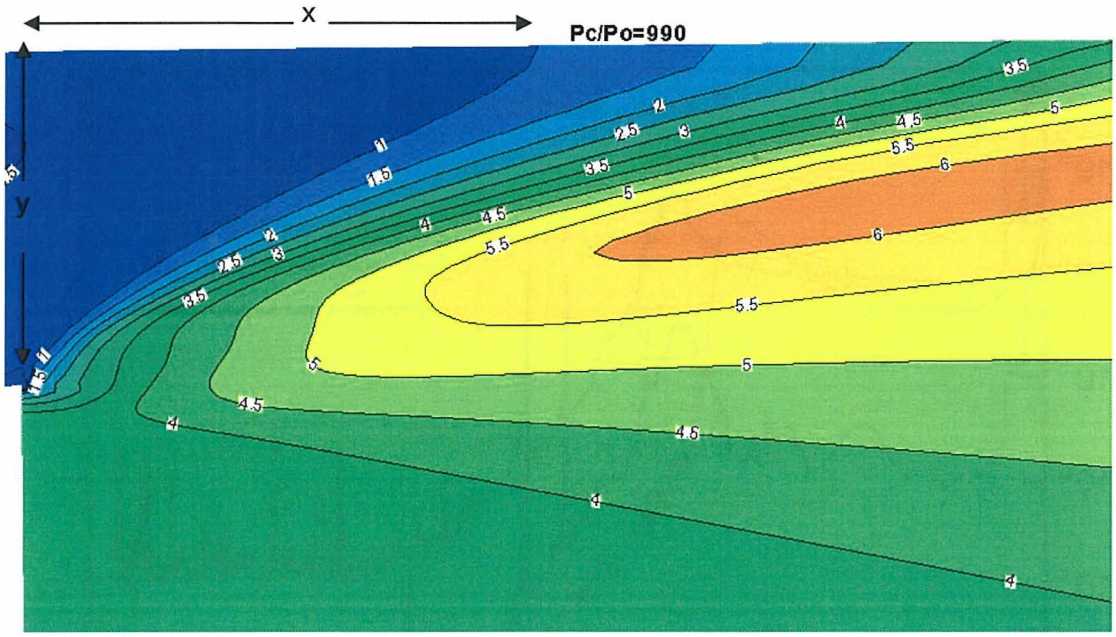

Fig. 7 Jet corner expansion Mach Contours

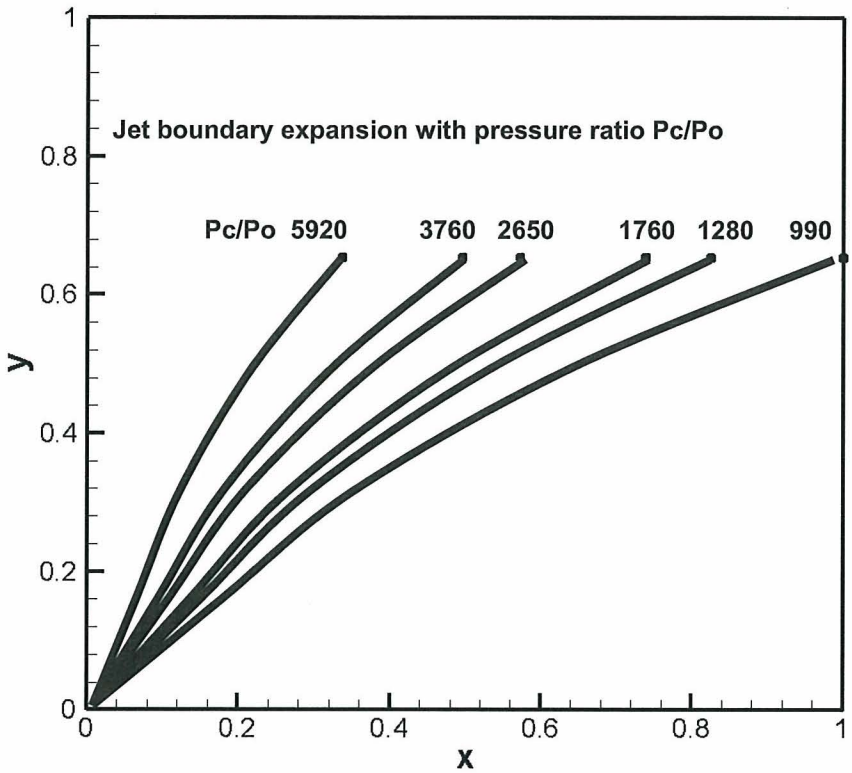

Fig. 8 Jet boundary expansion with pressure ratio, Pc/Po

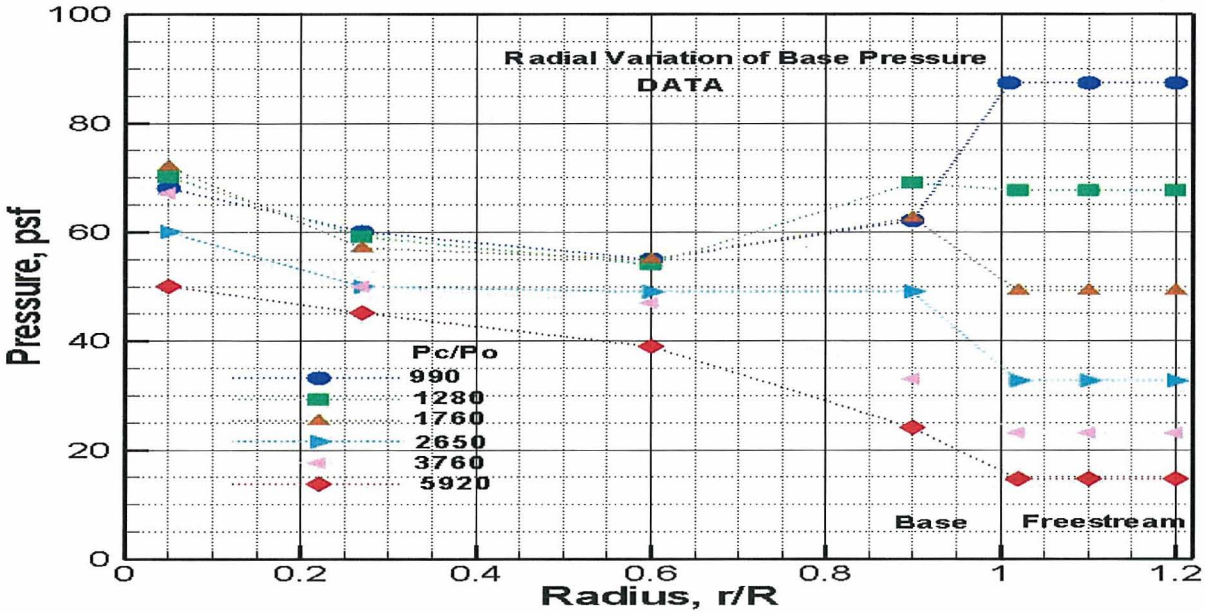

Fig. 9 Radial variation of base pressure with pressure ratio Pc/Po: Experimental Data

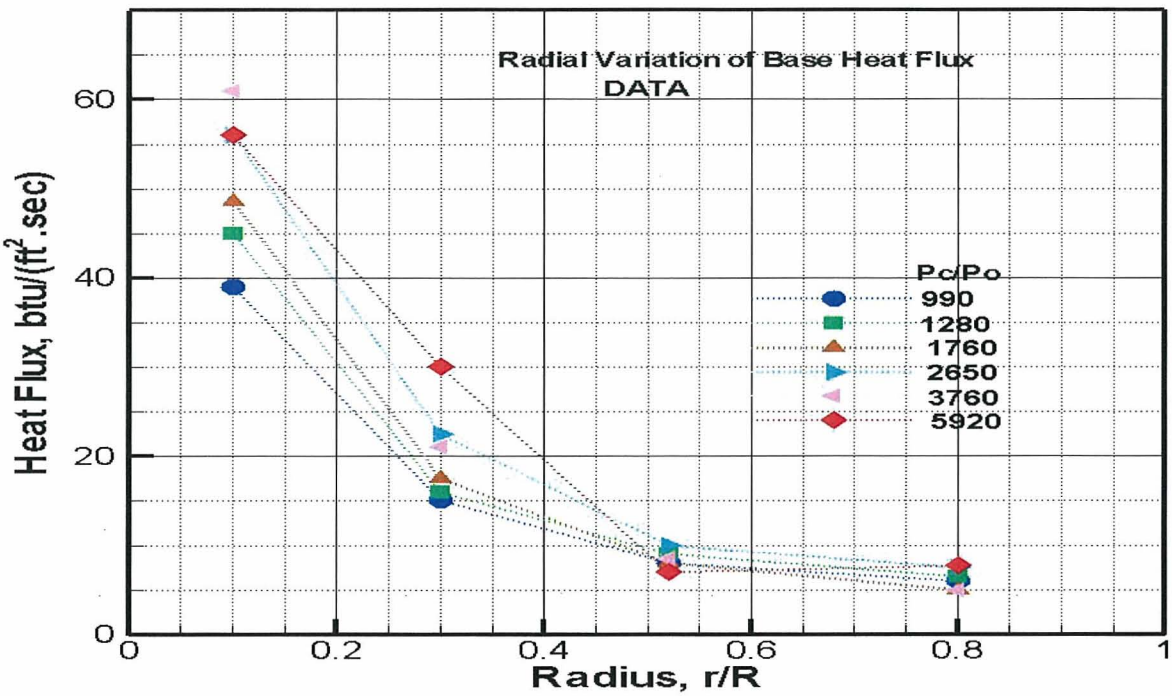

Fig.10 Radial variation of base heat flux with pressure ratio Pc/Po : Experimental Data

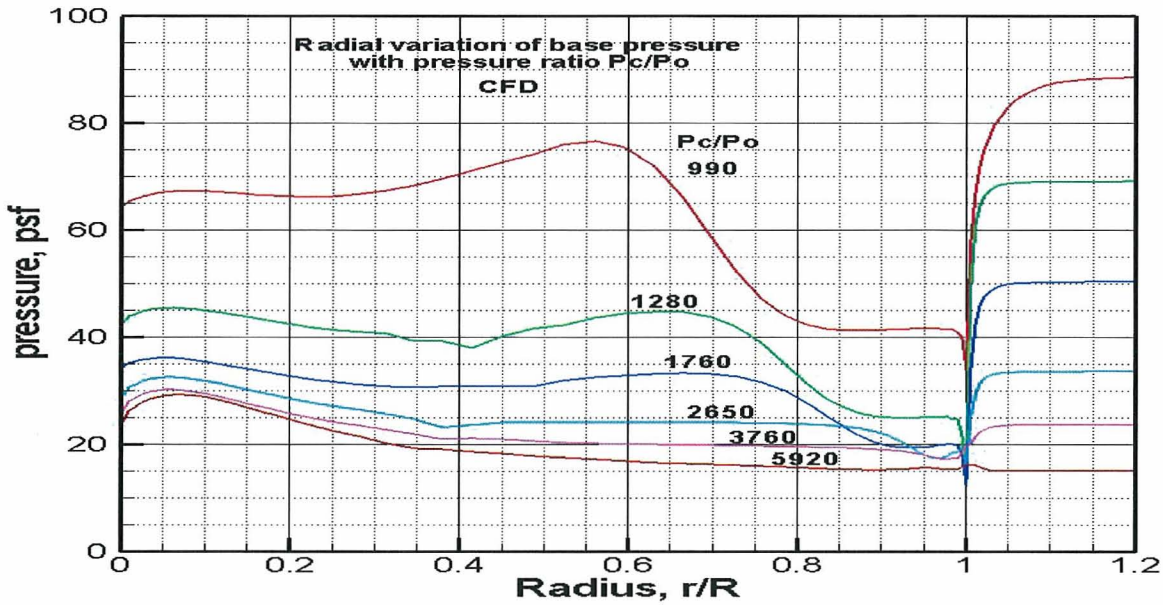

Fig. 11 Radial variation of base pressure with pressure ratio Pc/Po: Numerical solutions

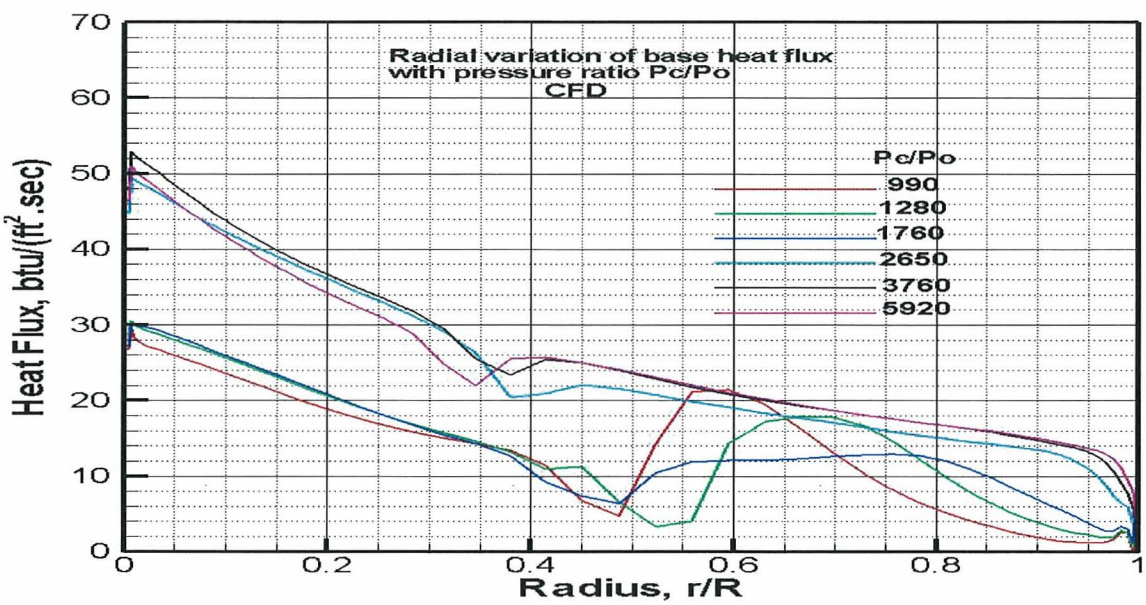

Fig. 12 Radial Variation of heat flux with pressure ratio Pc/Po: Numerical soutions

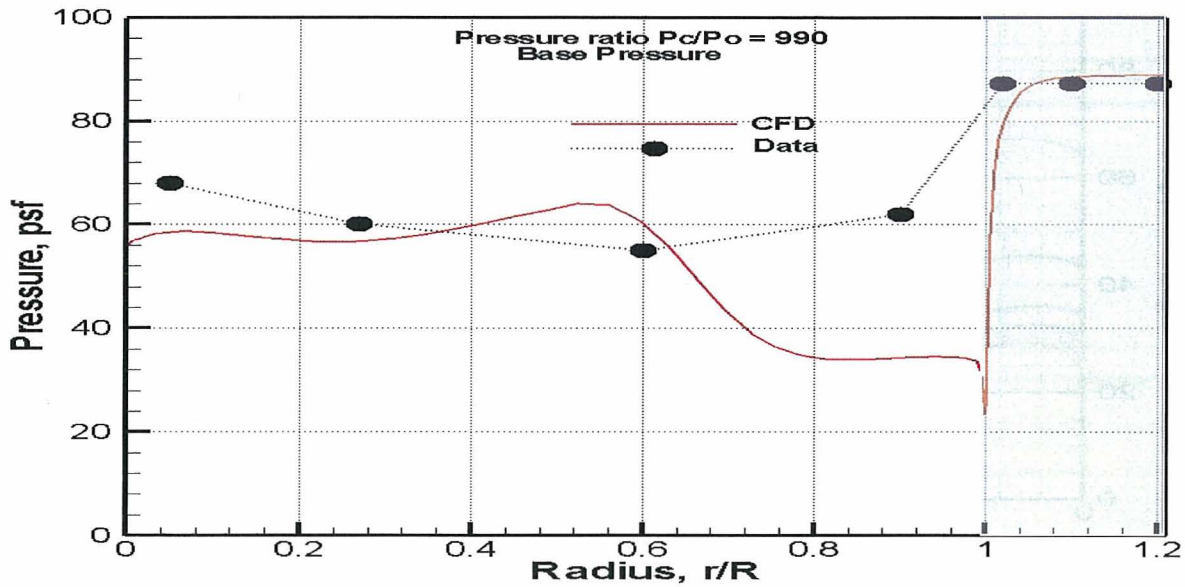

Fig. 13 Comparison of base pressure: CFD and Data for Pc/Po =990

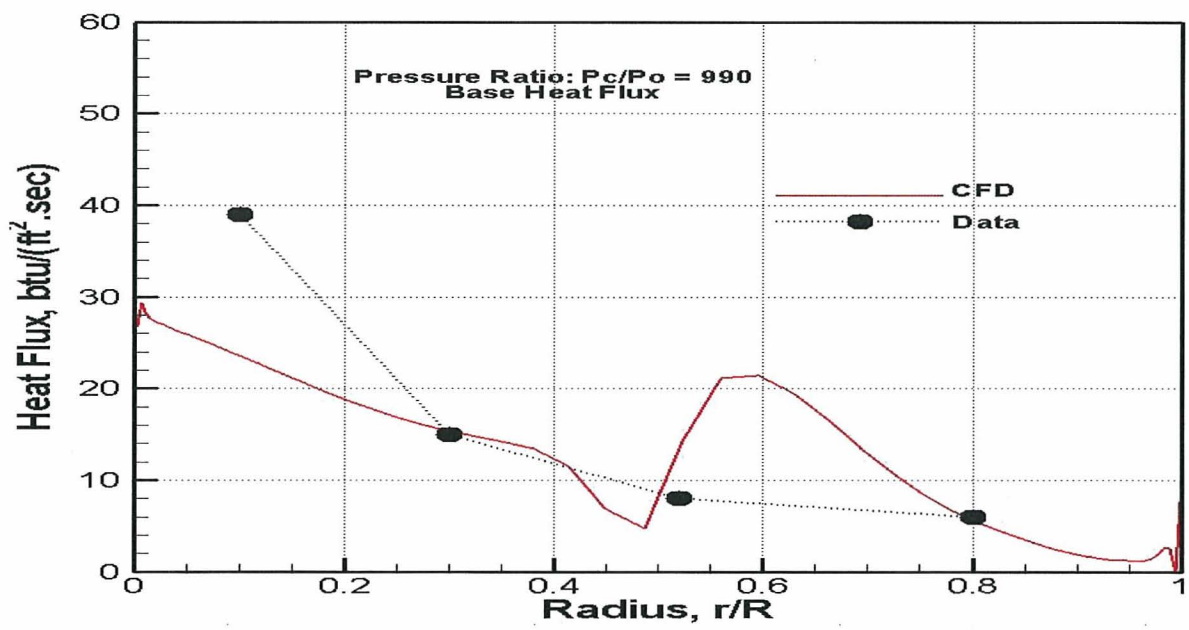

Fig. 14 Comparison of base heat flux: CFD and Data for Pc/Po =990

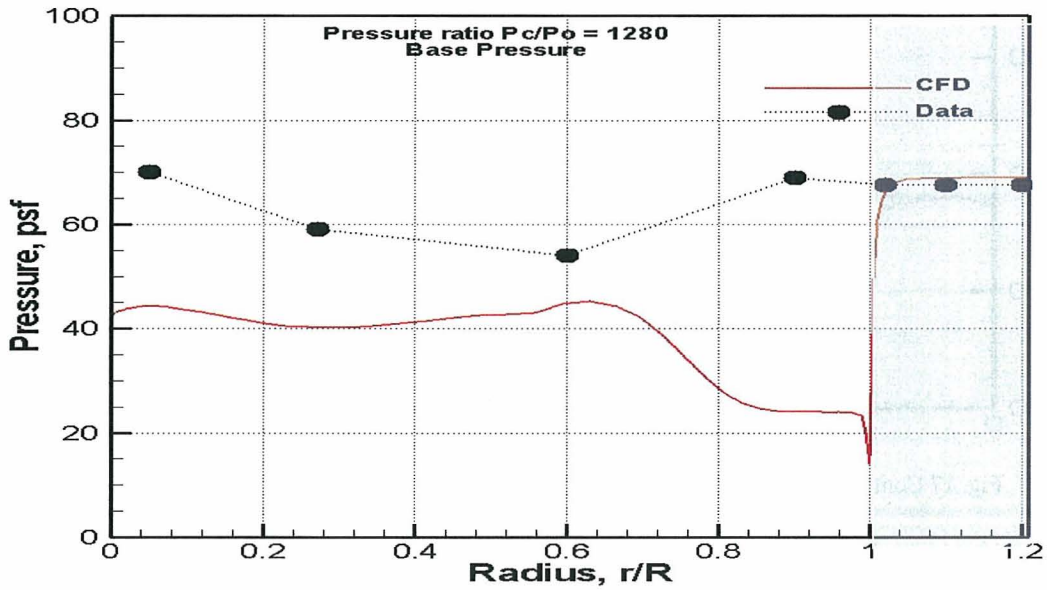

Fig. 15 Comparison of base pressure: CFD and Data for Pc/Po =1280

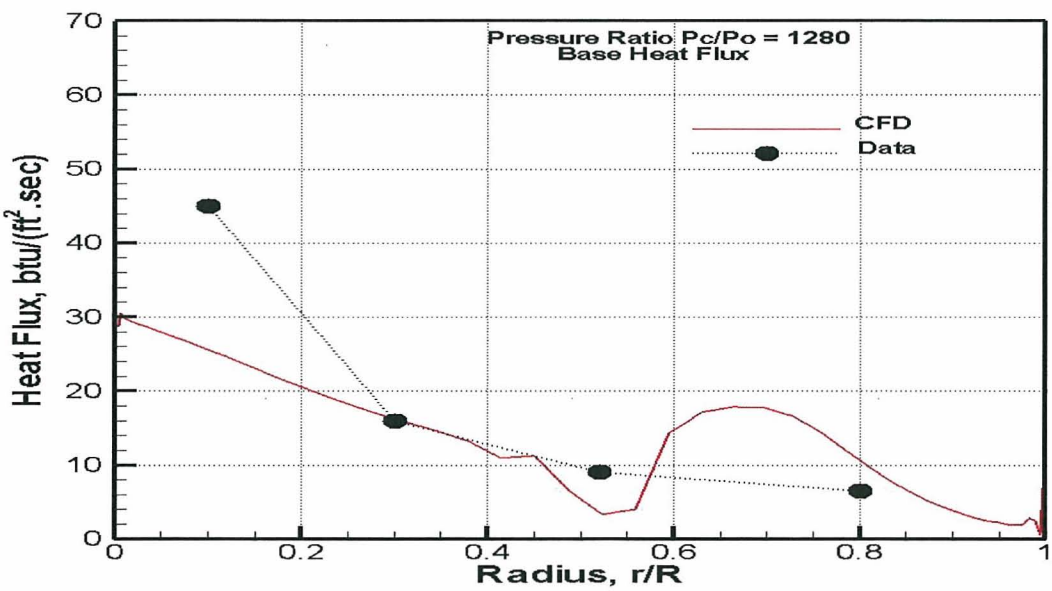

Fig. 16 comparison of base heat flux: CFD and Data for Pc/Po = 1280

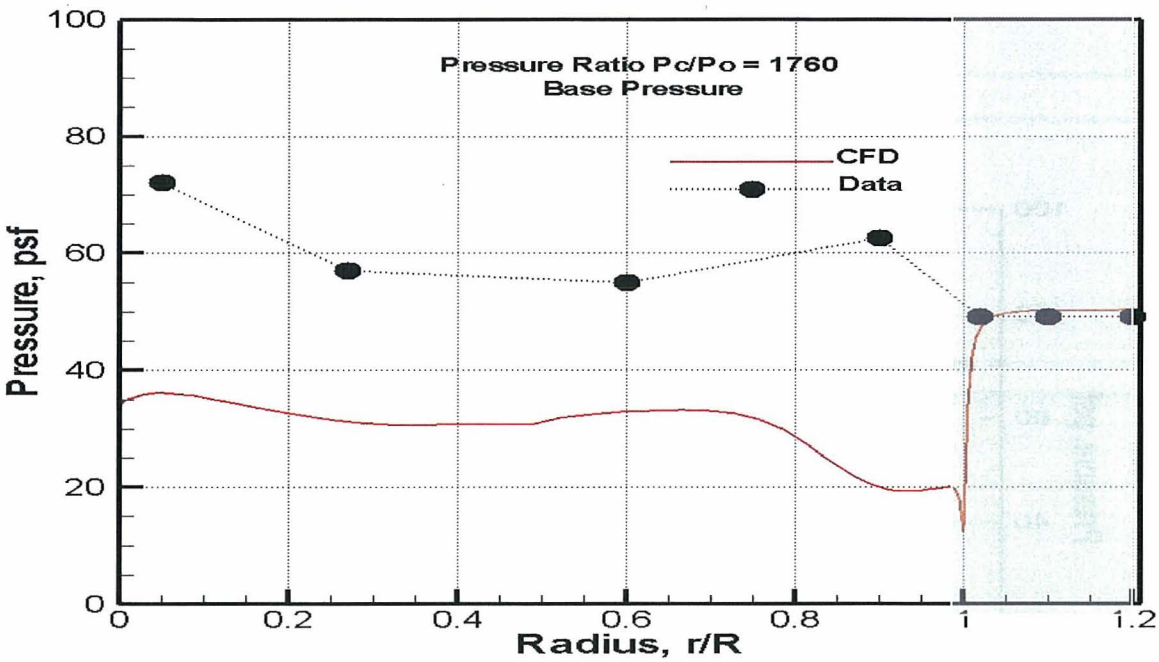

Fig. 17 Comparison of base pressure: CFD and data for Pc/Po = 1760

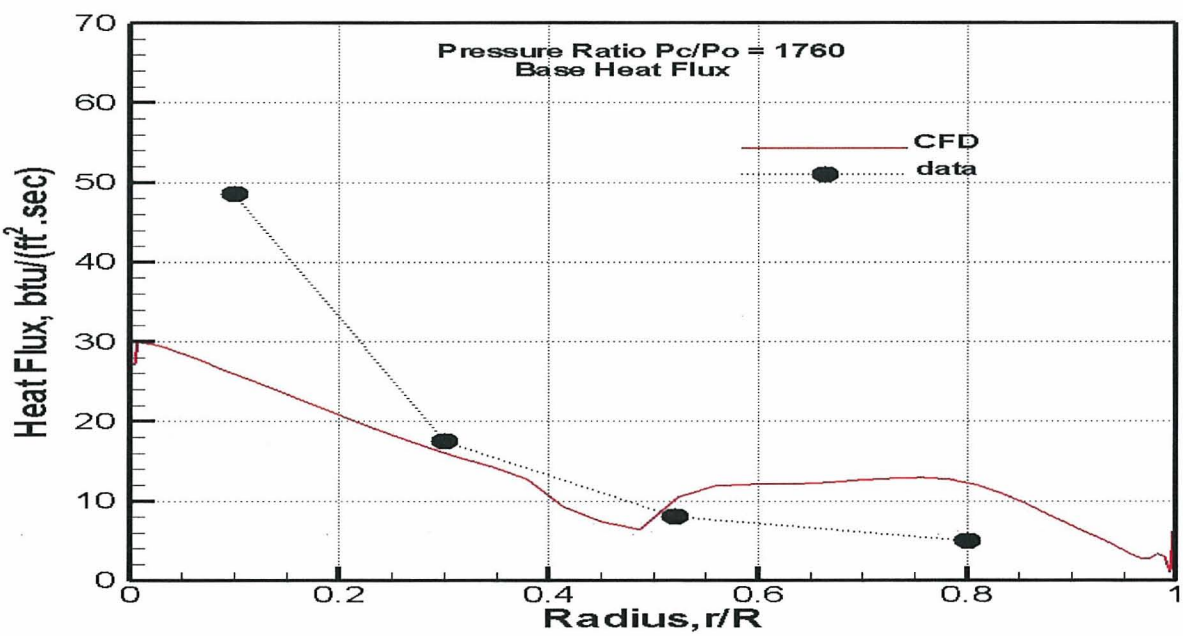

Fig. 18 Comparison of base heat flux: CFD and Data for Pc/Po =1760

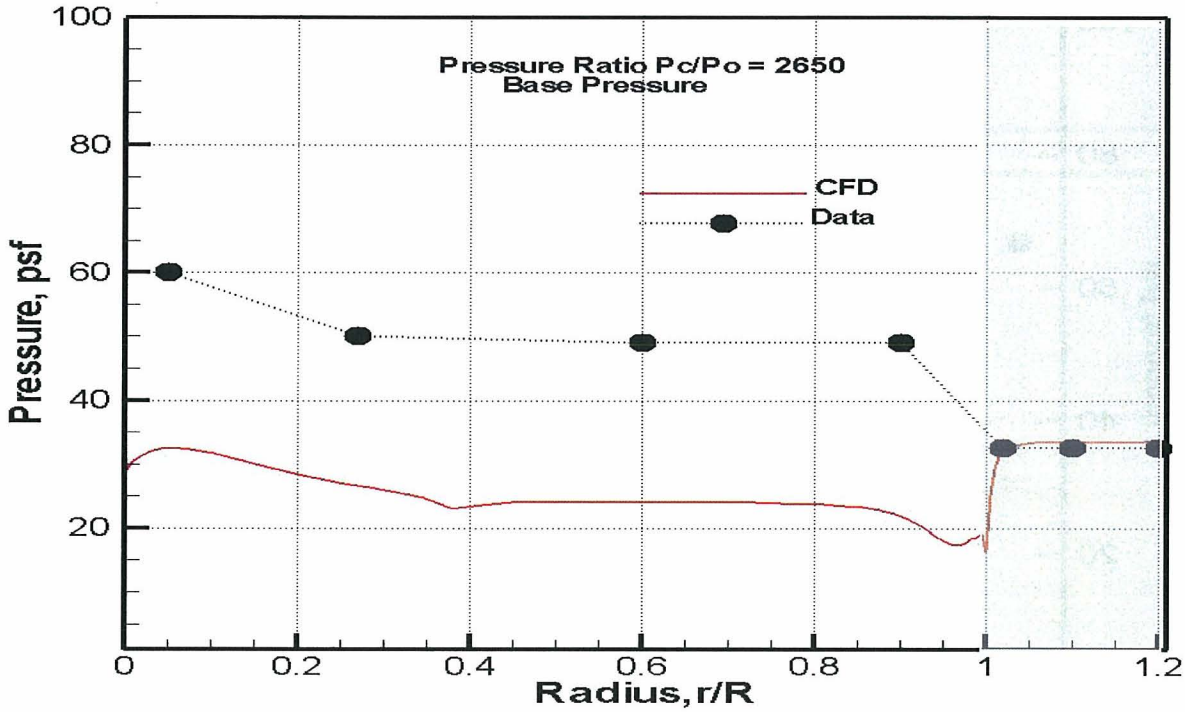

Fig. 19 Comparison of base pressure: CFD and Data for Pc/Po = 2650

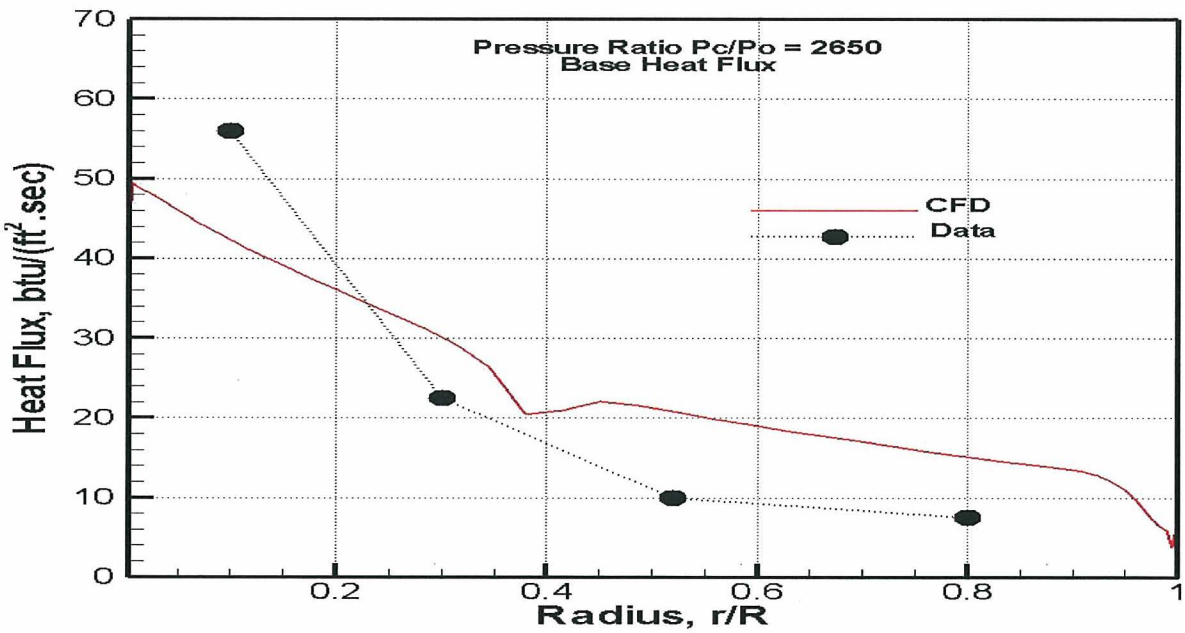

Fig. 20 Comparison of base heat flux: CFD and Data for Pc/Po =2650

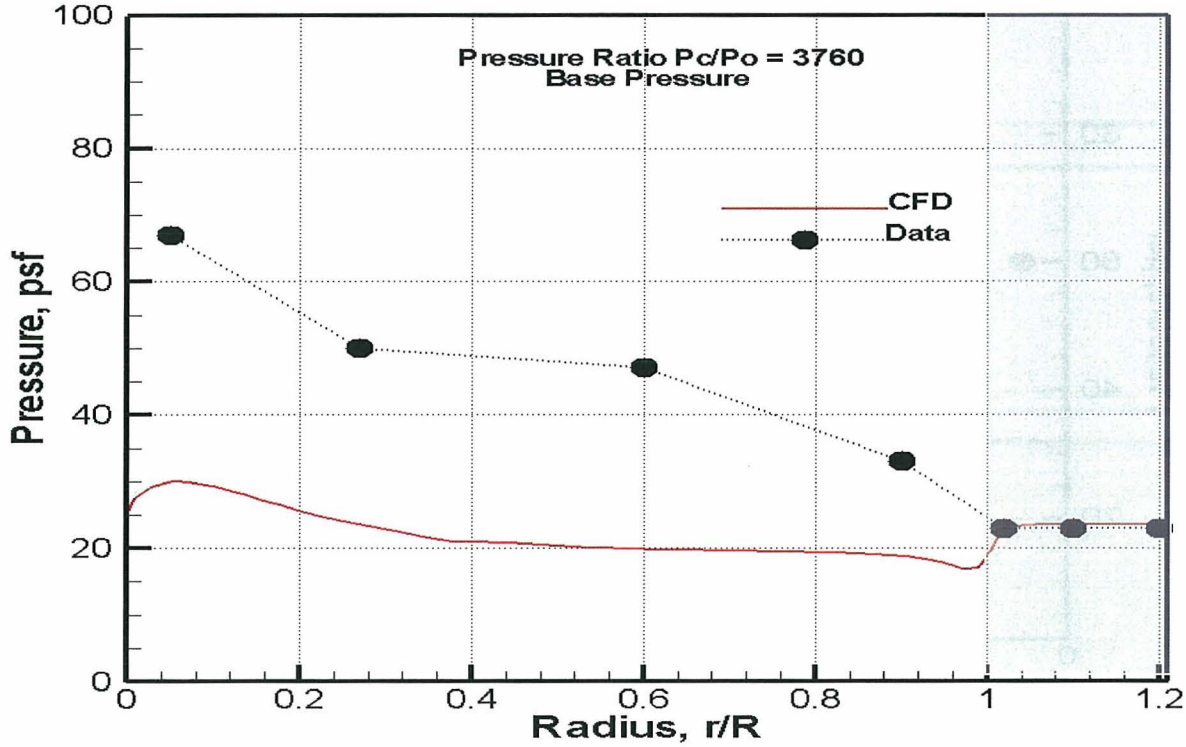

Fig. 21 Comparison of base pressure: CFD and Data for Pc/Po =3760

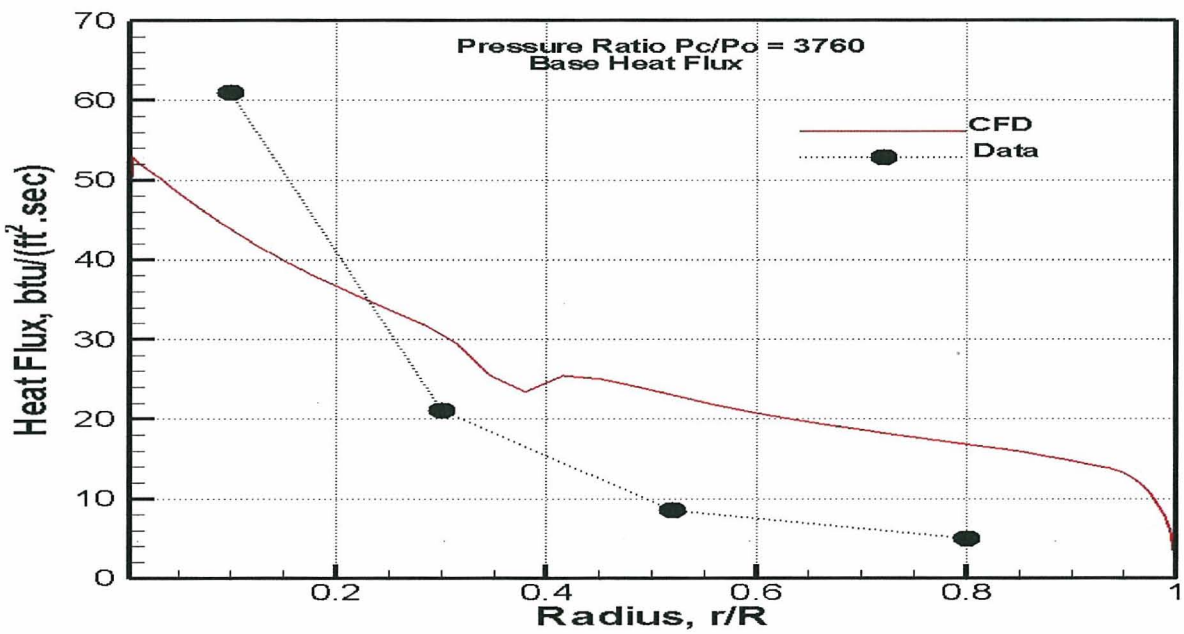

Fig. 22 Comparison of base heat flux: CFD and Data for Pc/Po =3760

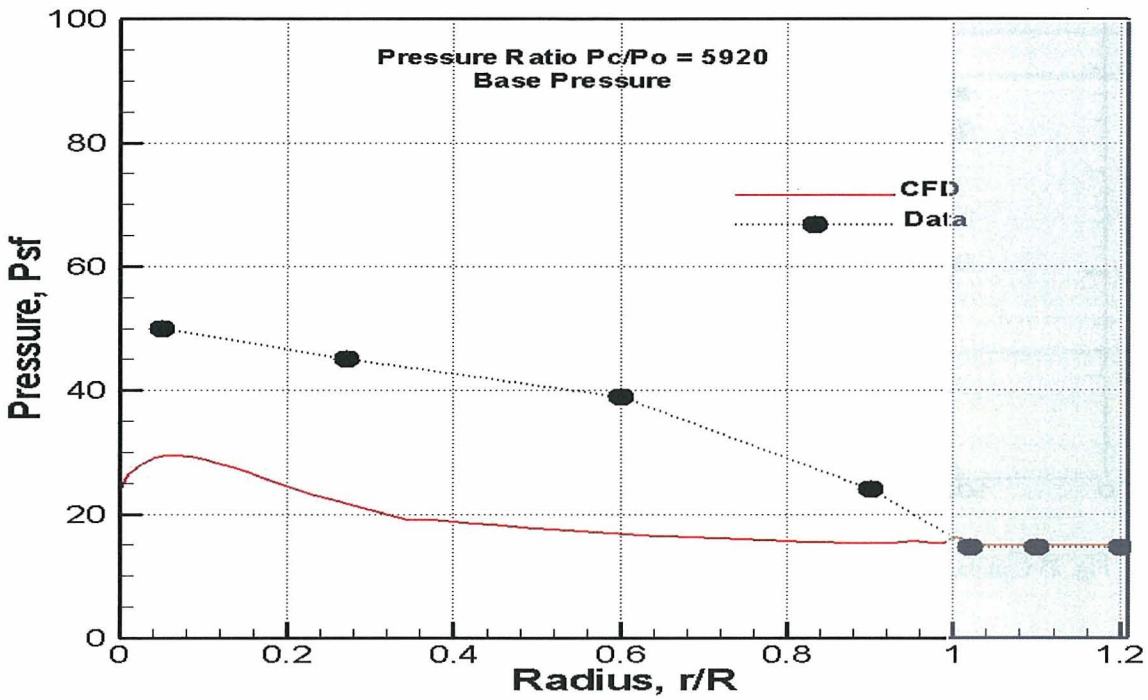

Fig. 23 Comparison of base pressure : CFD and Data for Pc/Po =5920

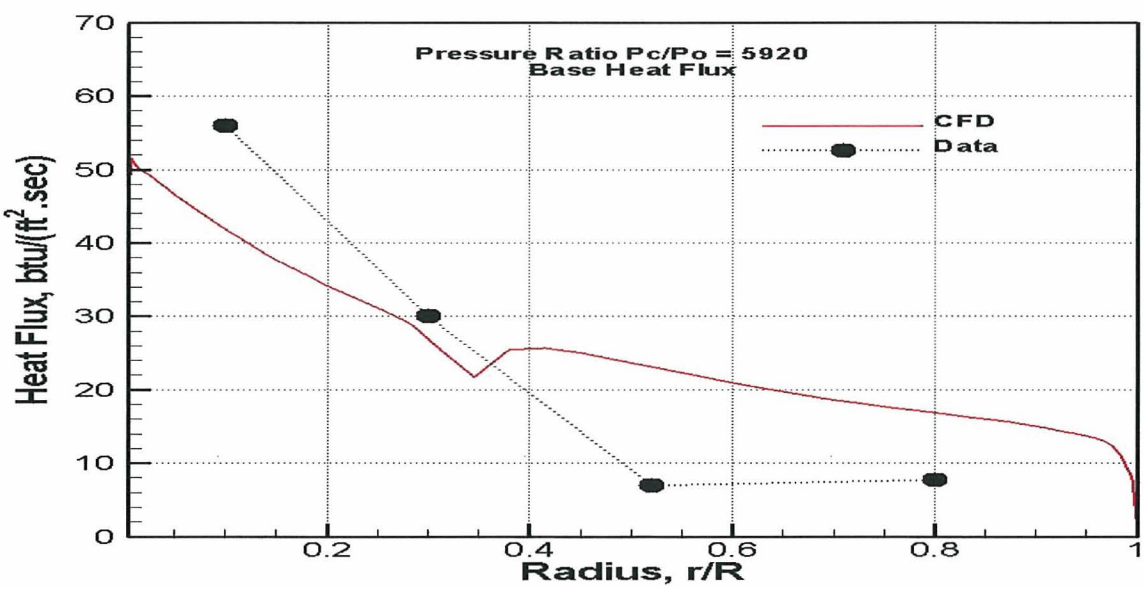

Fig. 24 Comparison of base heat flux: CFD and Data for Pc/Po =5920

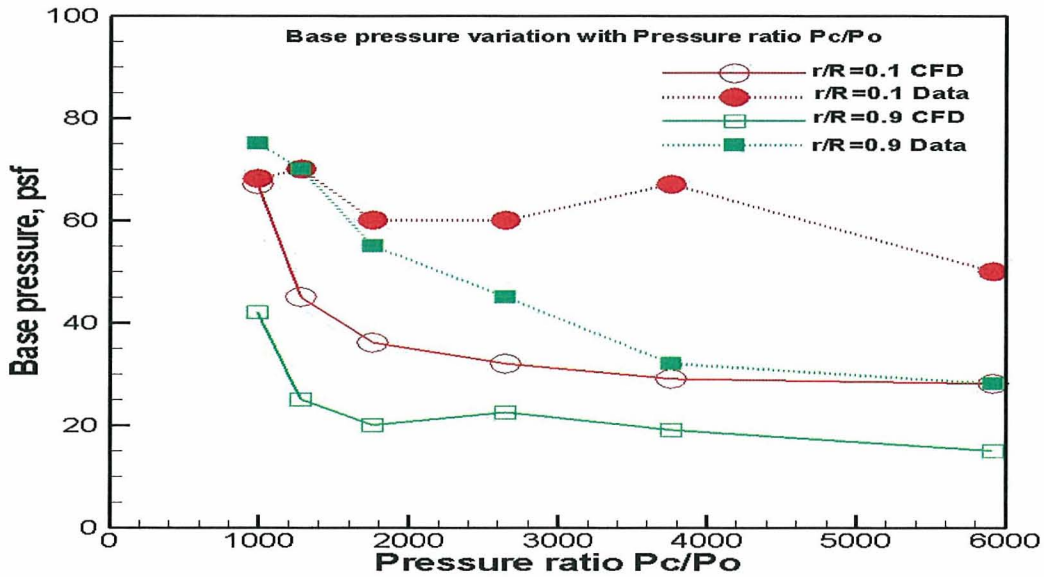

Fig. 25 Comparison of base pressure: CFD and Data with Pc/Po at r/R = 0.1 and 0.9.

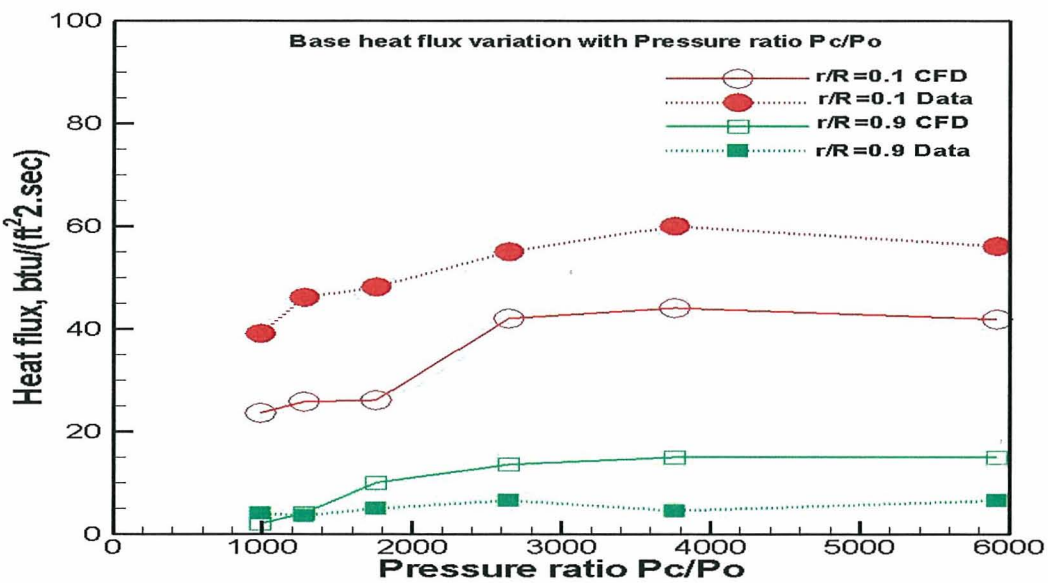

Fig. 26 Comparison of base heat flux: CFD and Data with Pc/Po at r/R = 0.1 and 0.9.

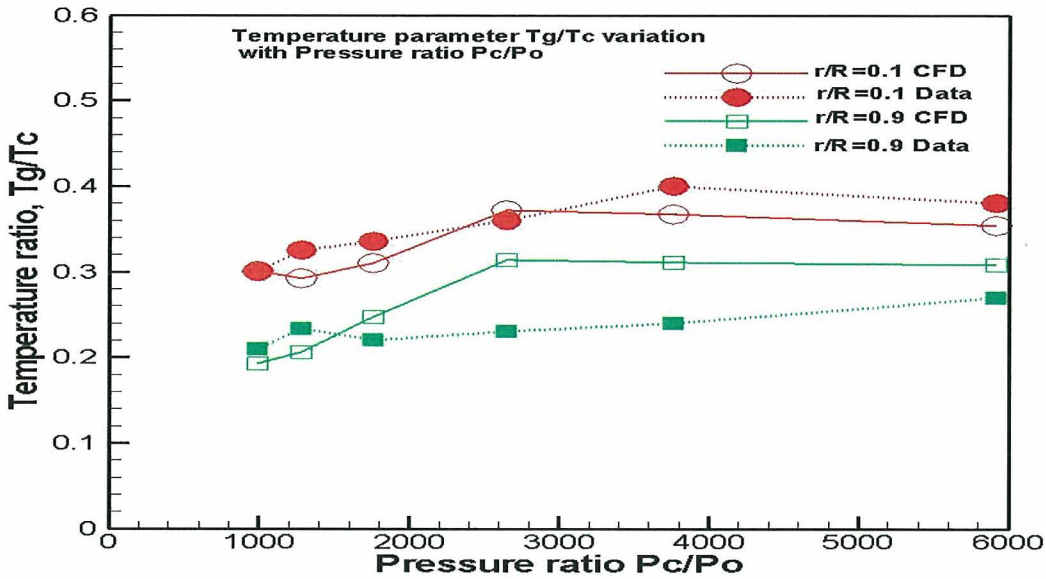

Fig. 27 Comparison of temperature parameter Tg/Tc: CFD and Data with Pc/Po at r/R = 0.1 and 0.9.

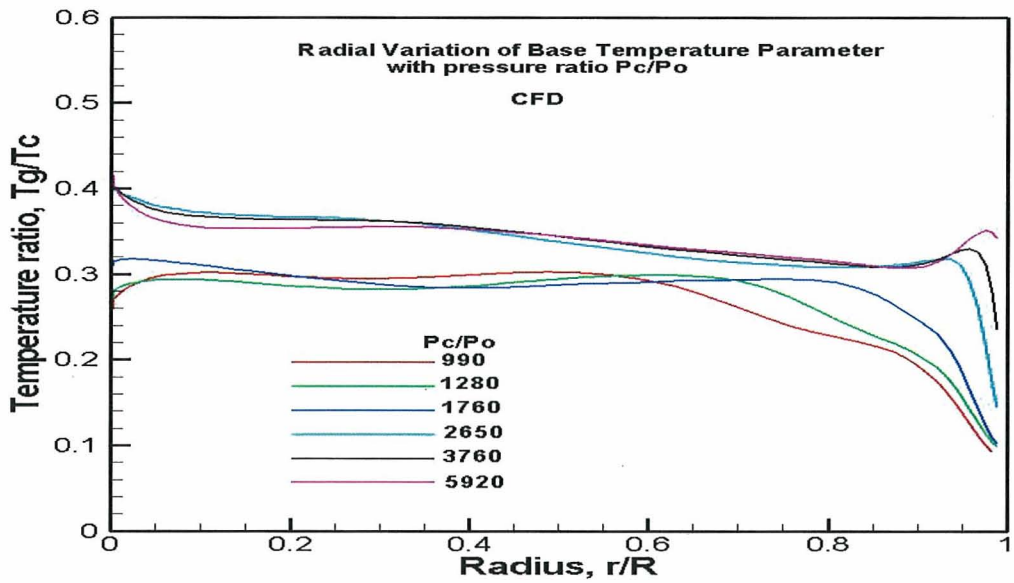

Fig. 28 Radial variation of base temperature parameter with Pc/Po : CFD

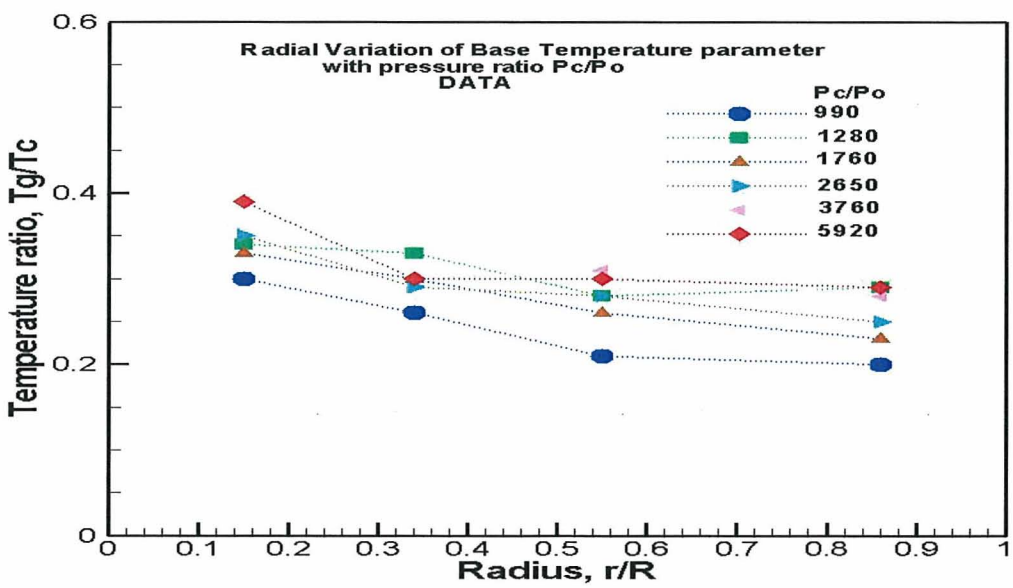

Fig. 29 Radial variation of base temperature parameter with Pc/Po : Data

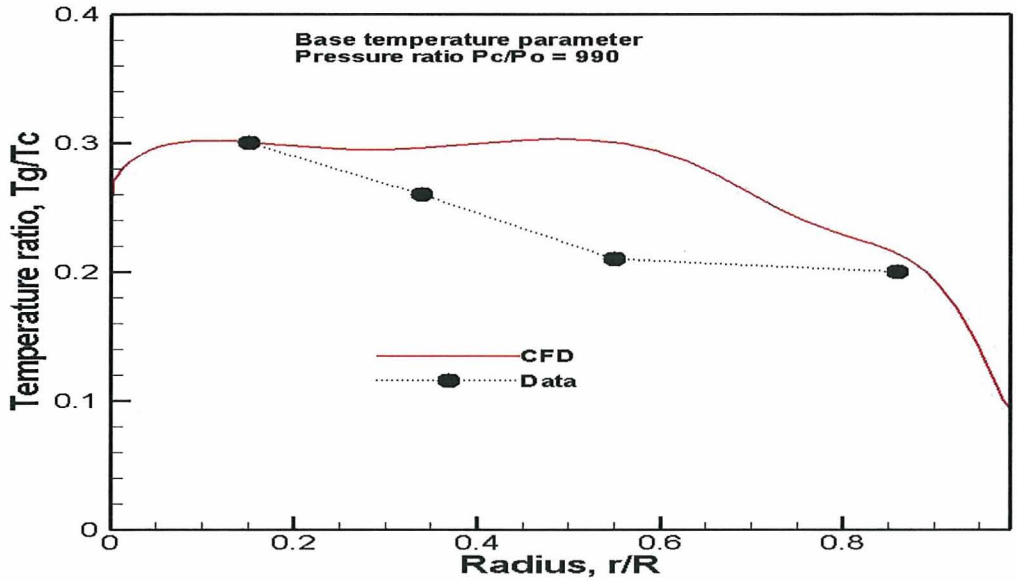

Fig. 30 Comparison of base temperature parameter: CFD and Data for Pc/Po = 990

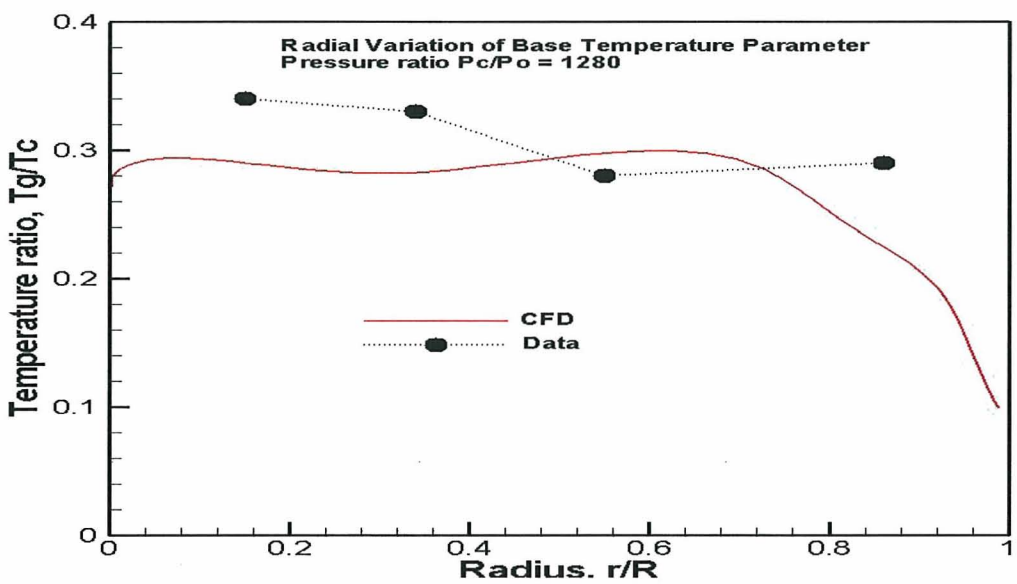

Fig. 31 Comparison of base temperature parameter: CFD and Data for Pc/Po = 1280

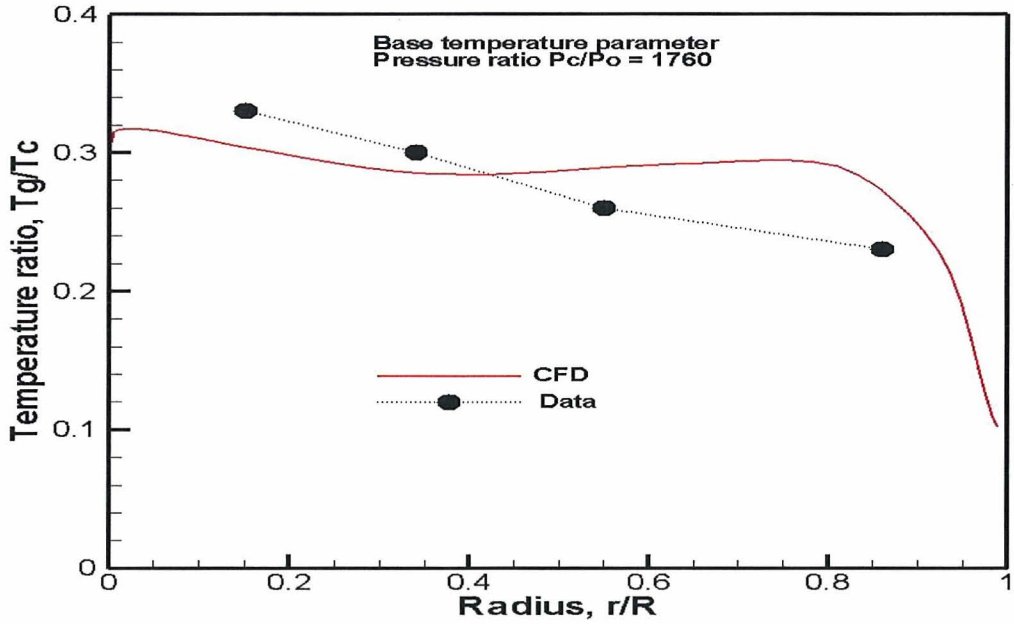

Fig. 32 Comparison of base temperature parameter: CFD and Data for Pc/Po = 1760

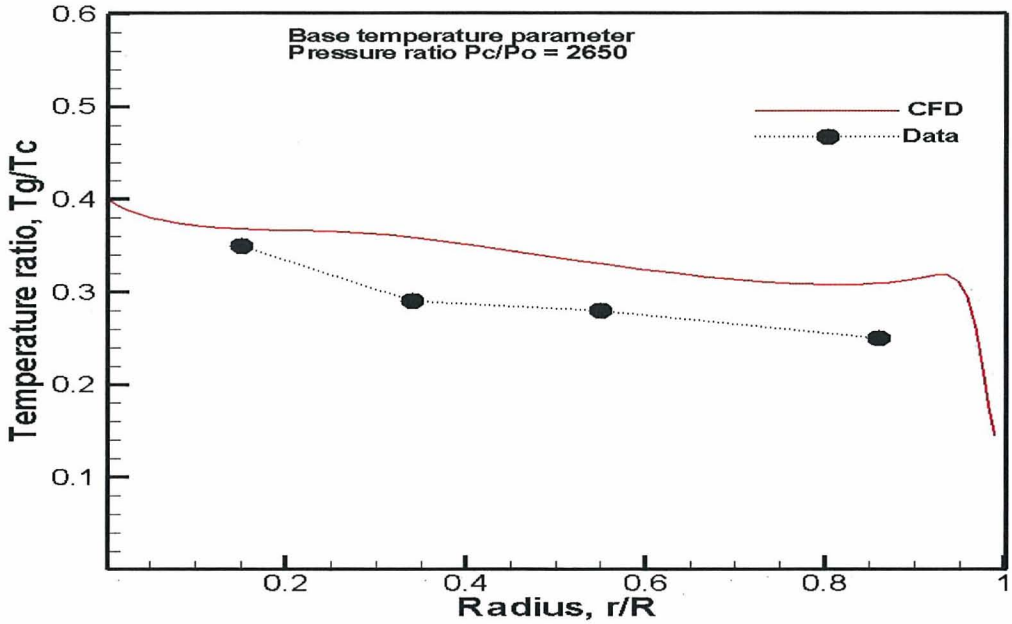

Fig. 33 Comparison of base temperature parameter: CFD and Data for Pc/Po = 2650

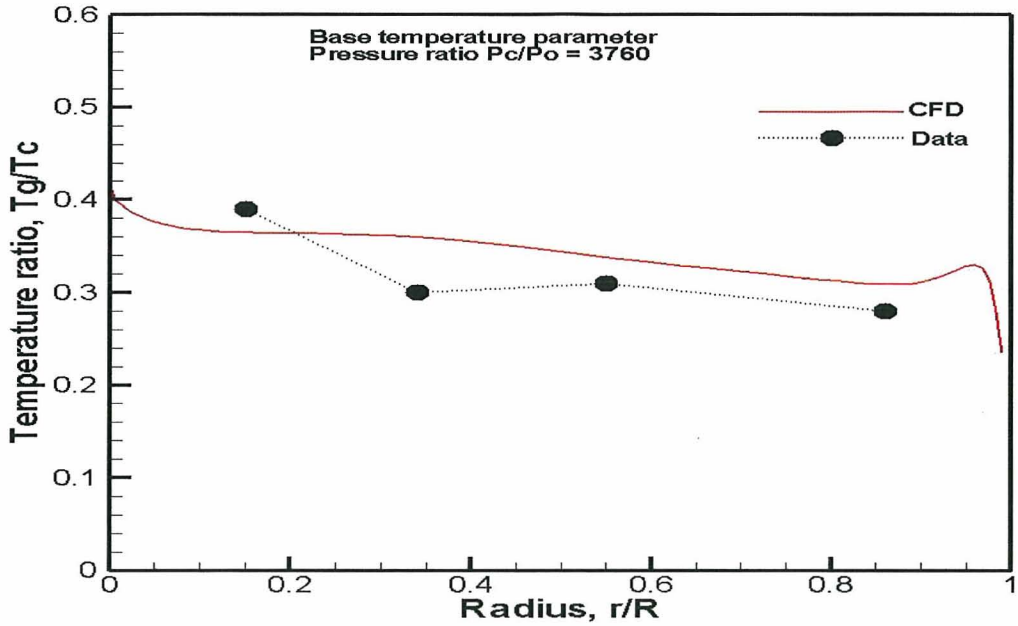

Fig. 34 Comparison of base temperature parameter: CFD and Data for Pc/Po = 3760

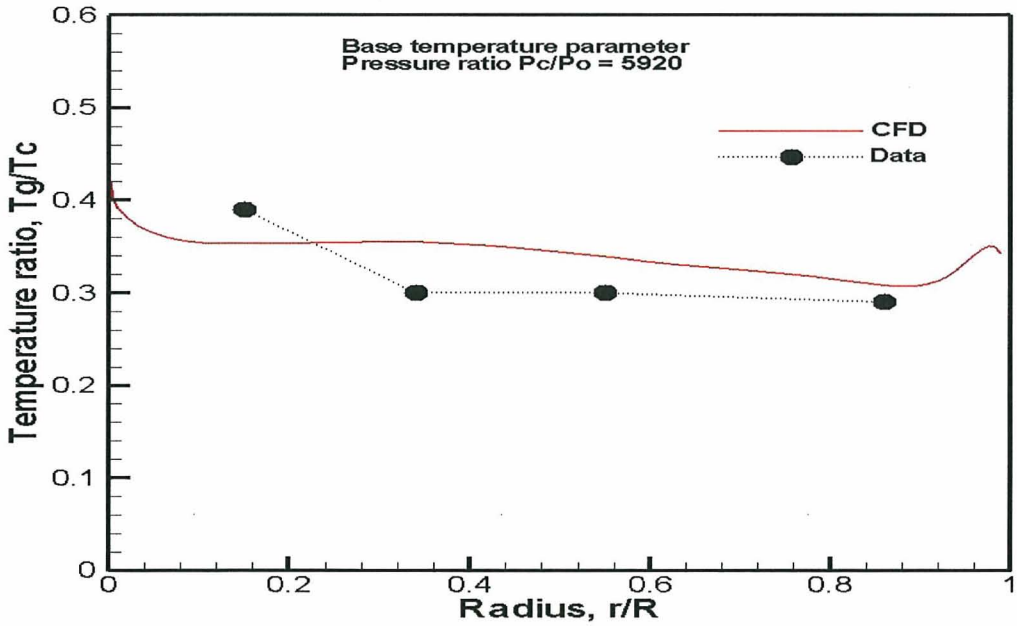

Fig. 35 Comparison of base temperature parameter: CFD and Data for Pc/Po = 5920